Hole Spin Qubits in Thin Curved Quantum Wells

Stefano Bosco* and Daniel Loss
Department of Physics, University of Basel, Klingelbergstrasse 82, Basel 4056, Switzerland

(Received 18 April 2022; revised 6 July 2022; accepted 19 September 2022; published 14 October 2022)

Hole spin qubits are frontrunner platforms for scalable quantum computers because of their large spin-orbit interaction that enables ultrafast all-electric qubit control at low power. The fastest spin qubits to date are defined in long quantum dots with two tight confinement directions, when the driving field is aligned to the smooth direction. However, in these systems the lifetime of the qubit is strongly limited by charge noise, a major issue in hole qubits. We propose here a different, scalable qubit design, compatible with planar CMOS technology, where the hole is confined in a curved germanium quantum well surrounded by silicon. This design takes full advantage of the strong spin-orbit interaction of holes, and at the same time suppresses charge noise in a wide range of configurations, enabling highly coherent, ultrafast qubit gates. While here we focus on a Si/Ge/Si curved quantum well, our design is also applicable to different semiconductors. These devices allow for ultrafast operations even in short quantum dots by a transversal electric field. This additional driving mechanism relaxes the demanding design constraints, and offers a way to reliably interface spin qubits in a single quantum dot to microwave photons. By considering state-of-the-art high-impedance resonators and realistic qubit designs, we estimate interaction strengths of a few hundreds of megahertz, largely exceeding the decay rate of spins and photons. Reaching such a strong coupling regime in hole spin qubits will be a significant step towards high-fidelity entangling operations between distant qubits, as well as fast single-shot readout, and could pave the way towards the implementation of a large-scale semiconducting quantum processor.

DOI: 10.1103/PhysRevApplied.18.044038

I. INTRODUCTION

Spin qubits in hole quantum dots are frontrunner candidates to process quantum information and implement large-scale universal quantum computers [1–8]. The key advantages of holes stem from their reduced sensitivity to the noise caused by hyperfine interactions to defects with nonzero nuclear spin [9–12], and from their strong effective spin-orbit interaction (SOI), which enables ultrafast and all-electric qubit control at low power [13–16].

The emergence of a large SOI in hole nanostructures is tightly linked to the design of the quantum dot, and it is maximized in systems where the hole is tightly confined in two directions and electrically driven by a field aligned to the softer confinement [17–20]. Rabi frequencies exceeding 400 MHz have been measured in germanium/silicon (Ge/Si) core-shell nanowires [14] and Ge hut nanowires [15]. A major issue in these systems, however, is the large coupling to charge noise that limits the coherence time of the qubit to tens of nanoseconds.

Moreover, the strong SOI in long hole quantum dots is predicted to enable a strong transversal [18] and longitudinal [21] coupling to high-impedance microwave resonators [22–27], where the strength of the interaction exceeds the coherence time of the qubits and the photons. Reaching the strong coupling regime in hole quantum dots will enable long-range connectivity of distant qubits [28] as well as quantum error correcting architectures [29], and will be a big step towards scaling up spin-based quantum computers. In contrast to state-of-the-art experiments, where multiple quantum dots encode a single qubit [30–35], hole spin qubits only need a single quantum dot [18,21,36,37], significantly diminishing the complexity of the architecture. However, to enhance the spin-photon interactions, the zero-point field of the photon needs to be aligned to the long direction of the dot [18,21], and thus the plunger electrode capacitively coupling the dot and the resonator has to be misaligned from the center of the dot, reducing the geometric lever arm to this gate and limiting the maximal spin-resonator coupling strength.

In this work, we propose a different type of hole spin qubit that is defined in a thin curved quantum well (CQW). This architecture is not only compatible with state-of-the-art material growth [38] and benefits from the large SOI of hole quantum dots, which can be attained at lower values of electric field, but it can also be designed to be free of charge noise. In contrast to alternative proposals to reduce the charge noise [39–41], in CQWs charge noise

*stefano.bosco@unibas.ch

is suppressed for a wide range of electric fields and not only at fine-tuned points in parameter space, providing a critical technological advantage compared to competing architectures.

The smallest coupling to charge noise occurs when the magnetic field is aligned to the well, where the effective Zeeman energy and the g-factor is widely tunable by external electric fields and by engineering the strain of the well. Strikingly, in an annular CQW, the maximal g-factor can reach rather large values, in analogy to topological insulator nanowires [42,43]. For this reason, CQWs can also be effective architectures in the search of exotic topological particles, such as Majorana fermions [44], where the low value of the g-factor along the hole nanowire is a critical issue [45].

Moreover, because of the large dipole moment of holes confined in CQWs, even spin qubits in short quantum dots can be driven ultrafast at low power by electric fields perpendicular to the smooth confinement direction. This mechanism not only relaxes the stringent technological constraints on the design of ultrafast spin qubits, but it also offers a different way to interface spin qubits in single quantum dots to microwave photons in high-impedance resonators, thus pushing spin-photon hybrid architectures towards higher speed and coherence standards, and helping in scaling up these architectures from linear arrays of quantum dots [46] to large-scale two-dimensional quantum processors [28,29].

This work is organized as follows. In Sec. II, we present the system and we introduce the theoretical model used to describe it, including an analysis of the strain, a crucial ingredient in hole nanostructures [47–49]. We discuss two different setups: an annular CQW, where a semiconducting shell fully covers an inner core [38], and a CQW grown on top of a planar substrate. The latter architecture, in particular, is compatible with current CMOS processes, and it holds particular promise for scaling up quantum computers. As the complete theoretical model is rather complicated, to gain valuable insights into the response of the system, in Sec. III, we derive an effective low-energy theory for the CQW, and discuss its key features in the presence of electric and magnetic fields. The effective model introduced in this section describes with a reasonable accuracy a wide range of devices, when additional valence bands as well as lattice and cross-section anisotropies are also included. These effects are addressed in Appendices C and D, respectively. In Secs. IV and V, we analyze in detail hole spin qubits in these systems and we discuss qubits in quantum dots that are short and long compared to the radius of the well, respectively. We highlight the advantages of these qubits compared to alternative designs and we also examine the differences between annular and planar CQWs. In Sec. VI, we analyze the coupling between these qubits and photons in microwave resonators. We estimate that the interaction strength in state-of-the-art devices can exceed a few hundreds of megahertz, much larger than the decay rate of qubits and photons, thus enabling a strong qubit-photon coupling, with far-reaching consequences for spin-based quantum computing.

II. HOLES IN CURVED QUANTUM WELLS

A. Setup

In this work, we analyze the CQWs sketched in Fig. 1. We examine setups where the hole wave function is confined in an annular CQW (pink) sandwiched between a core of radius R_1 and an outer shell (blue) extending from a radius R_2 to R_3. We introduce the thickness $\tau = R_2 - R_1$ and the average radius $R = (R_1 + R_2)/2$ of the quantum well. The well extends along the z direction and the $x = r\cos\varphi$ and $y = r\sin(\varphi)$ directions define the cross section; r and φ are polar coordinates. The spin qubit is defined by confining the hole in a quantum dot along z and by further applying a magnetic field $\mathbf{B}$ that splits the spin states. While for simplicity in this work we focus on electrostatically defined quantum dots [4,14], we point out that better control over the size and shape of the dot could be reached by growing thin insulating regions in the quantum well [50].

For the most part of our analysis, we explicitly study annular CQWs where a thin semiconducting shell fully surrounds an inner core, as shown in Fig. 1(a). We emphasize that the growth of this structure has been experimentally demonstrated in Ref. [38]. However, our theory also describes well architectures comprising planar CQWs grown on a planar substrate, as shown in Fig. 1(b), as well as CQWs with less symmetric cross sections, e.g., square

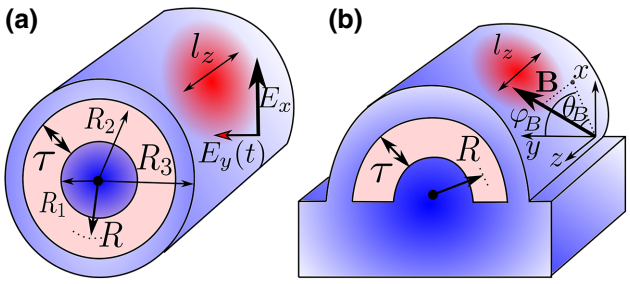

FIG. 1. Sketch of a hole spin qubit in a curved quantum well. The hole wave function is confined in the pink region in the (x, y) plane, and it extends for a harmonic length l_z in the z direction. External electric and magnetic fields are also indicated. The blue regions highlight the interface with a different material. In particular, an experimentally relevant example comprises a germanium thin quantum well (pink) surrounded by silicon (blue). In (a) we show an annular CQW, where a thin semiconducting shell fully surrounds an inner core. In (b) we show a CQW in a planar setup, where the semiconducting shell is grown on top of a planar substrate.

or hexagonal; see Appendix D. In particular, planar architectures grown on top of a silicon substrate hold particular promise to scale up quantum processors because of their compatibility with CMOS technology [51]. We envision linear arrays of quantum dots defined in individual CQWs, in analogy to Ref. [46], that can be coupled to each other via resonators [28,29].

In this context, another material that is attracting much attention is strained Ge, which presents large SOI, small effective mass, and can be grown epitaxially with high purity on top of Si [1]. Moreover, in nanowires the mismatch of the energy bands between Si and Ge and the alignment of their Fermi energies ensures that even without external gating, the charge carriers are holes confined in Ge [1]. For these reasons, although our theory is applicable to a wide range of semiconducting materials, we restrict ourselves to the analysis of a Ge CQW (where the hole is confined) surrounded by Si. The confinement of the holes in the shell rather than in the core has far-reaching consequences on the resulting spin qubits, and sets our setup apart from current Ge/Si core-shell and hut nanowires [14,15,52].

B. Theoretical model

The physics of hole nanostructures is accurately described by the Hamiltonian

$$H = H_{\mathrm{LK}} + V_{\mathrm{C}}(r,z) - e\mathbf{E}\cdot\mathbf{r} + H_{\mathbf{B}} + H_{\mathrm{BP}}. \tag{1}$$

The kinetic energy of the holes is modeled by the isotropic Luttinger-Kohn (LK) Hamiltonian [53]

$$H_{\mathrm{LK}} = \left(\gamma_1 + \frac{5}{2}\gamma_s\right)\frac{p^2}{2m} - \frac{\gamma_s}{m}(\mathbf{p}\cdot\mathbf{J})^2, \tag{2}$$

where γ_1 and γ_s are material-dependent LK parameters parametrizing the mixture of heavy holes (HHs) and light holes (LHs) at the top of the valence band of cubic semiconductors, $\mathbf{p} = -i\hbar\nabla$ is the canonical momentum [$p^2 = -\hbar^2\nabla^2$], and $\mathbf{J} = (J_x, J_y, J_z)$ is the vector of spin-3/2 matrices. In particular, in Ge $\gamma_1 \approx 13.35$ and we use the isotropic LK approximation with $\gamma_s = (\gamma_2 + \gamma_3)/2 \approx 4.96$ [53]. Deviations from this model, including the contributions of the additional valence band and of cubic anisotropies, are addressed in AppendicesC and D, respectively. The quantum dot is defined by the confinement potential $V_C(r,z) = V_r(r) + \hbar\omega_z z^2/2l_z^2$, comprising an abrupt potential $V_r(r)$ in the radial direction modeling the boundary of the CQW and a smooth harmonic potential parametrized by a characteristic length l_z and frequency $\omega_z = \hbar\gamma_1/ml_z^2$.

We also include an electric field $\mathbf{E}$ produced by the gates and a magnetic field $\mathbf{B}$, which couples to the spin of the hole by the Hamiltonian

$$\frac{H_{\mathbf{B}}}{2\mu_B} = \kappa\mathbf{B}\cdot\mathbf{J} + \frac{\gamma_s}{\hbar}\left[\left(\frac{\gamma_1}{\gamma_s} + \frac{5}{2}\right)\{\mathbf{A},\mathbf{p}\} - 2\{\mathbf{A}\cdot\mathbf{J}, \mathbf{p}\cdot\mathbf{J}\}\right], \tag{3}$$

where $\{A,B\} = (AB + BA)/2$ and $\mu_B = e\hbar/2m$ is the Bohr magneton. Here, $H_{\mathbf{B}}$ includes the Zeeman field and the orbital magnetic field effects coming from the Peierls substitutions $\mathbf{p} \to \boldsymbol{\pi} = \mathbf{p} + e\mathbf{A}$ with $\mathbf{A} = (zB_y - yB_z/2, -zB_x + xB_z/2, 0)$. We neglect small corrections $\mathcal{O}(\mathbf{B}^2)$ and anisotropies $\propto J_i^3$ of the Zeeman interactions.

C. Strain in a Ge curved quantum well

Another key feature to understand the hole nanostructure is strain that can strongly influence the behavior of hole spins confined in quantum dots [47–49]. For example, in planar Ge heterostructures and Ge hut wires, strain favors HHs [54,55], resulting in a large g-factor when B is perpendicular to the substrate, and orders of magnitude smaller g-factors otherwise [1,56]; a HH ground state also yields a weaker SOI, cubic in momentum, and slower Rabi oscillations [20]. In contrast, Ge/Si core-shell nanowires are characterized by a strain favoring a LH ground state, thus strongly suppressing the anisotropy of the g-factor and enhancing the speed of the Rabi oscillations [17,47]. Here, we show that in CQWs, strain can be engineered to favor HHs or LHs depending on the thickness of the quantum well.

We restrict ourselves to the analysis of the technologically relevant scenario where a thin Ge CQW is surrounded by Si [38]. In this case, the strain is mainly determined by the mismatch of lattice constants of Si and Ge, $a_{\mathrm{Si}} = 0.543$ nm and $a_{\mathrm{Ge}} = 0.566$ nm, respectively. In the annular Ge CQW sketched in Fig. 1(a), strain is accurately modeled by the Bir-Pikus (BP) Hamiltonian

$$H_{\mathrm{BP}} = J_z^2\epsilon_z - J_r^2\epsilon_r, \tag{4}$$

where $J_r = J_x\cos(\varphi) + J_y\sin(\varphi)$ is the spin-3/2 matrix aligned to the radial direction. The strain energies ϵ_r and ϵ_z can be approximated as

$$\epsilon_r \approx \left(1 - \frac{\tau}{2R}\right)^2 |b|\varepsilon_0 > 0, \tag{5a}$$

$$\epsilon_z \approx \left(\frac{1}{2} - \frac{\tau}{8R} - \frac{R^2}{R_3^2}\right)\frac{\tau}{R}|b|\varepsilon_0, \tag{5b}$$

where $\varepsilon_0 \approx 1.6\varepsilon_\parallel$ is the typical strain in planar heterostructure [57], $\varepsilon_\parallel = (a_{\mathrm{Ge}} - a_{\mathrm{Si}})/a_{\mathrm{Ge}} \approx 4\%$ is the relative mismatch of lattice constants of Si and Ge, and $b = -2.2$ eV [53]. If Ge is grown on pure Si, the typical strain energy is $|b|\varepsilon_0 \approx 140$ meV. However, if a $Si_{1-x}Ge_x$ compound [1] substitutes pure Si in the core and outer shell,

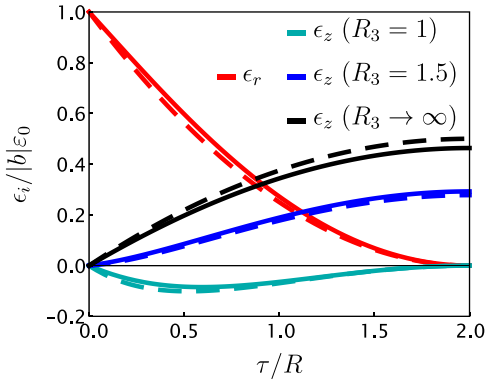

FIG. 2. Strain energy of a Ge CQW as a function of thickness τ of the well. With dashed lines we show the approximated results in Eqs. (5), while with solid lines we show a more general result, including differences in the elastic constants of Si and Ge, as discussed in Appendix A. The radial strain ϵ_r is to good approximation independent of the outer Si shell, while the longitudinal strain ϵ_z strongly depends on the outer shell thickness R_3, measured with respect to R_2; see Fig. 1. For Ge CQWs, the radial strain dominates, while the longitudinal strain plays a significant role in thicker Ge wells, especially when covered by a thick outer Si layer.

the strain decreases as $\varepsilon_\parallel \to (1-x)\varepsilon_\parallel$. The dependence of these quantities on the thickness τ of the Ge well is shown in Fig. 2. By comparing to the results obtained by a more general analysis analogous to Ref. [47], we observe that the simple expressions in Eqs. (5) accurately describe the system. A more detailed derivation of Eqs. (4) and (5), also including a discussion on inhomogeneous strain, is provided in Appendix A.

From Eq. (4), we observe that the strain energy can be decomposed into two different components, parametrized by the competing energies $\epsilon_{r,z}$, that can be engineered independently. In particular, the energy ϵ_z favors holes with the quantization axis aligned to the z direction, and it strongly depends on the thickness τ of the Ge well and on the radius R_3 of the outer Si shell. When R_3 is sufficiently large (small) then $\epsilon_z > 0$ ($\epsilon_z < 0$) and the LHs (HHs) have a lower energy. When $\epsilon_z > 0$, this term is qualitatively analogous to the typical strain in Si/Ge core-shell nanowires [47], where the BP Hamiltonian is [58]

$$H_{\rm BP}^{c/s} \approx J_z^2 \frac{|b|\varepsilon_0}{2}\left(1 - \frac{R_1^2}{R_2^2}\right). \tag{6}$$

In contrast, the energy ϵ_r favors HHs in the radial direction, and to good approximation it is independent of the presence of the outer Si shell. This type of strain is not present in usual Ge/Si core-shell nanowires, but it emerges in planar heterostructures [20,40,55] and hut wires [54]. When $\tau \ll R$, we recover this expected limit and

$$H_{\rm BP}^{\rm PH} = -J_r^2 |b|\varepsilon_0. \tag{7}$$

From Fig. 2, we observe that, while ϵ_z is dominant at large values of the ratio τ/R, in thin Ge CQWs ϵ_r is the dominant contribution and the ground state comprises to good approximation radial HHs.

In the following, we restrict ourselves to the analysis of devices with thin Ge CQWs and a thick outer Si layer, such that $\epsilon_r > \epsilon_z > 0$.

D. Hamiltonian in cylindrical coordinates

In a thin Ge CQW, the radial confinement energy

$$\epsilon_c = \frac{\hbar^2\pi^2\gamma_1}{m\tau^2} \approx 100 \times \left(\frac{10\ \text{nm}}{\tau}\right)^2 \text{meV} \tag{8}$$

is large compared to the quantization energy $\hbar\omega_\varphi = \hbar^2\gamma_1/mR^2$ of the total angular momentum and to the confinement energy $\hbar\omega_z = \hbar^2\gamma_1/ml_z^2$ along the quantum well, both in the millielectron volt range. In this case, where $\tau \ll R, l_z$, the dynamics of the confined holes is well described by an effective low-energy theory where the radial degrees of freedom are frozen.

However, because the radial strain ϵ_r is comparable to the radial confinement, i.e., $\epsilon_c \sim \epsilon_r \sim 100$ meV, an accurate low-energy model of the system needs to account exactly for ϵ_r. For this reason, we rotate the Hamiltonian in Eq. (1) to a cylindrical coordinate system where the spin quantization axis is aligned to the radial direction and the radial strain $-\epsilon_r J_r^2$ is diagonal. This rotation is generated by the angular-dependent unitary operator $U = e^{-iJ_3\varphi}e^{-iJ_2\pi/2}$. To avoid confusion, in the transformed frame we label the spin-3/2 matrices by 1,2,3 instead of x, y, z.

The effect of U on the most relevant operators is

$$U^\dagger \mathbf{p} U = \mathbf{p} + \hbar \mathbf{e}_\varphi J_1, \tag{9a}$$

$$U^\dagger \mathbf{J} U = \mathbf{e}_r J_3 + \mathbf{e}_\varphi J_2 - \mathbf{e}_z J_1. \tag{9b}$$

We note that in the product of the rotated operators, some care must be taken because $\mathbf{e}_{r,\varphi}$ are unit vectors in cylindrical coordinates that depend on φ, and do not commute with $p_\varphi = -i\hbar\partial_\varphi$. For this reason, we report in Appendix B the explicit expressions of the LK and BP Hamiltonians in this coordinate system.

Importantly, from Eqs. (9), it follows that the total angular momentum $F_z = p_\varphi + \hbar J_z$ in the original coordinate system transforms as

$$U^\dagger F_z U = p_\varphi, \tag{10}$$

in the transformed frame. Consequently, the physical eigensolutions of the Hamiltonian in the rotated frame are antiperiodic in φ and p_φ is quantized in units of $(2l-1)\hbar/2$ with $l \in \mathbb{Z}$.

III. EFFECTIVE LOW-ENERGY THEORY

We first derive an effective model describing the band dispersion in the absence of external fields ($\mathbf{E} = \mathbf{B} = 0$) and then generalize our results to account for finite values of $\mathbf{E}$ and $\mathbf{B}$. In the frame introduced in Sec. II D and when $\mathbf{E} = \mathbf{B} = 0$, p_φ and p_z are good quantum numbers of the total isotropic Hamiltonian H in Eq. (1). To construct an effective Hamiltonian that acts only on these two degrees of freedom, we trace out the radial direction by projecting the rotated H onto the basis states

$$\psi_n(r) = \sqrt{\frac{2}{\tau r}} \sin\left[\frac{\pi n}{\tau}\left(r - R - \frac{\tau}{2}\right)\right], \qquad n \in \mathbb{N}, \quad (11)$$

satisfying hard-wall boundary conditions at $r = R \pm \tau/2$. These functions are the eigenstates of the operator $\gamma_1 p_r^2/m$ to eigenvalues $\epsilon_c n^2$, with $p_r = -i\hbar(\partial_r + 1/2r)$ being the Hermitian radial momentum, and they provide a complete basis for the radial degree of freedom.

The quasidegenerate ground state of the system comprises two HH Kramers partners with quantum number $n = 1$, energetically separated from the first (HH) excited states by the energy $3\epsilon_c(1 - 2\gamma_s/\gamma_1)/2$, and from the second (LH) excited state by $2\gamma_s\epsilon_c/\gamma_1 + 2\epsilon_r + \epsilon_z$. By considering only the first two radial eigenstates with $n = 1$ and $n = 2$, and by a second-order Schrieffer-Wolff transformation [53,59], we find that the dynamics of the ground state is captured by the quadratic Hamiltonian

$$H_{\rm GS} = \frac{p_+ p_-}{2m^*} - \frac{p_+^2 + p_-^2}{4\delta m} + \sigma_+(v_- p_- - v_+ p_+) + \text{H.c.}, \quad (12)$$

where $p_\pm = p_\varphi/R \pm i p_z$ and H.c. means Hermitian conjugate. The parameters of the effective theory to second order in τ/R are given by

$$\frac{1}{m^*} \approx \frac{1}{m}(\gamma_1 + \gamma_s - 3\tilde{\gamma}), \quad (13a)$$

$$v_- \approx \frac{3}{2}\frac{\hbar}{mR}\left[(\gamma_s - \tilde{\gamma}) - \frac{1}{2}(\gamma_1 + 2\gamma_s)\tilde{\epsilon}_z\right], \quad (13b)$$

$$\frac{1}{\delta m} \approx \frac{3}{m}\gamma_s\tilde{\epsilon}_z, \quad \text{and} \quad v_+ \approx \frac{3}{4}\frac{\hbar}{mR}\gamma_1\tilde{\epsilon}_z; \quad (13c)$$

we introduce here the dimensionless quantities

$$\tilde{\gamma} = \frac{256}{9\pi^2}\frac{\gamma_s}{10 + \gamma_1(3\epsilon_c + 4\epsilon_r + 2\epsilon_z)/\gamma_s\epsilon_c}, \quad (14a)$$

$$\tilde{\epsilon}_z = \frac{\epsilon_z}{\epsilon_z + 2\epsilon_r + 2\gamma_s\epsilon_c/\gamma_1}. \quad (14b)$$

We emphasize that while in this work we focus on Si/Ge/Si quantum wells, whose growth is demonstrated in Ref. [38], the results presented are also qualitatively valid for other possible semiconductors supporting holes described by the LK and BP Hamiltonians, including, for example, GaAs, InAs, and InSb. In particular, the formulas in Eqs. (13) are also directly applicable in these cases, provided that the appropriate material-dependent parameters γ_1, γ_s, κ, and b are used [53].

While $\tilde{\gamma}$ only quantitatively modifies the parameters of the effective Hamiltonian, the longitudinal strain $\tilde{\epsilon}_z$ introduces the qualitatively different terms v_+ and δm that modify the SOI and the effective mass along the quantum well and in the angular direction. The dependence of these parameters on strain is shown in Fig. 3. We observe that, while the effective mass is not strongly affected by δm, the effective SOI can be largely modified by ϵ_z, and v_+ can become comparable to v_-.

The effective theory in Eq. (12) can also be generalized to include the high-energy valence band that is separated in energy from the HH-LH subspace by an energy $\Delta_S \approx 300$ meV. These high-energy states do not qualitatively alter the physics described here. In fact, in this case, Eq. (12) is still valid, but the effective parameters in Eqs. (13) acquire corrections that scale as Δ_S/ϵ_c. The effect of the additional valence band is discussed in detail in Appendix C, and in particular, the generalized versions of Eqs. (13) are given in Eqs. (C1).

In Fig. 4(a) we compare the energy dispersion of the lowest-energy levels as a function of p_z derived from the effective model in Eq. (12) to the dispersion calculated by numerically diagonalizing the Hamiltonian H in Eq. (1). For the numerical calculations, we project H onto the lowest 20 states $\psi_n(r)$ in the radial direction [see Eq. (11)], and consider 40 total angular momentum eigenstates. We observe excellent agreement between effective theory and the numerics even at rather large values of momentum p_z, strain $\epsilon_{r,z}$, and thickness τ.

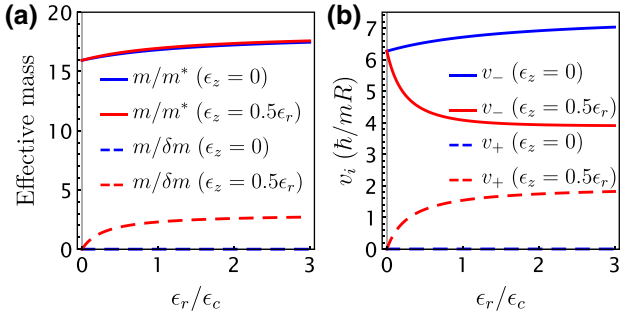

FIG. 3. Parameters of the effective theory in Eq. (12) of a thin Ge CQW. We show with blue and red lines the inverse effective mass and the spin-orbit velocities [see Eqs. (13)] obtained at $\epsilon_z = 0$ and at $\epsilon_z = 0.5\epsilon_r$, respectively. While the effective mass is not strongly modified by strain, the SOI can acquire a large strain dependence, and it significantly varies as a function of the longitudinal strain ϵ_z.

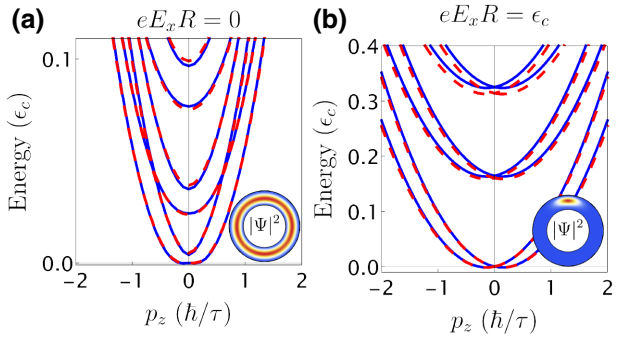

FIG. 4. Energy dispersion of a strained thin Ge CQW. We compare the dispersion calculated from the effective theory in Eq. (12) (blue lines) and by numerically diagonalizing the Hamiltonian H in Eq. (1) (red dashed lines). In (a) and (b), we show results obtained at $E_x = 0$ and $E_x = \epsilon_c/eR$. We consider $\mathbf{B} = 0$, $\tau = R/2$, $\epsilon_r = 2\epsilon_z = 3\epsilon_c$. In the insets at the bottom right of the figures, we show the hole density of the ground state at $p_z = 0$ in the lab frame. At $p_z = 0$, in (a) the ground and first excited states are spilt by the small SOI gap Δ [Eq. (17)]. In contrast, in (b) the gap $\hbar\omega_E$ [Eq. (21)] is large and E_x pins the hole to the top of the well.

At $p_z = 0$, the eigenstates of the effective Hamiltonian $H_{\rm GS}$ in Eq. (12) are the degenerate Kramers partners

$$|g^l_{1,2}\rangle = \frac{|\uparrow\rangle \mp |\downarrow\rangle}{\sqrt{2}}|\pm l\rangle \quad \text{and} \quad |e^l_{1,2}\rangle = \frac{|\uparrow\rangle \pm |\downarrow\rangle}{\sqrt{2}}|\pm l\rangle, \tag{15}$$

where $|\uparrow\downarrow\rangle$ are the pseudospins and $|\pm l\rangle$ are the total angular momentum eigenstates with eigenvalues $p_\varphi|\pm l\rangle = \pm\hbar(l - 1/2)|\pm l\rangle$ for $l \in \mathbb{N}$. The eigenenergies are

$$\epsilon_{g,e} = \frac{\hbar^2(2l-1)^2}{8m_\varphi R^2} \mp \frac{\hbar}{2R}(v_- - v_+)(2l-1), \tag{16}$$

where the angular mass is $m_\varphi = (1/m^* - 1/\delta m)^{-1} = m/[\gamma_1 + \gamma_s - 3(\tilde\gamma + \gamma_s\tilde\epsilon_z)]$; see Eqs. (13); neglecting the small effect of strain, we find that $m_\varphi \approx 0.06m$, thus resulting in a variation of the angular mass of 20% from the average value m/γ_1.

The ground state of the system comprises the Kramers doublet $|g^{l=1}_{1,2}\rangle$, and is separated from the first excited doublet $|e^{l=1}_{1,2}\rangle$ by the SOI energy

$$\Delta = \frac{\hbar}{R}v_\varphi = \frac{3}{2}\frac{\tilde\kappa}{\gamma_1}\hbar\omega_\varphi, \tag{17}$$

where we introduce the angular SOI velocity $v_\varphi = v_- - v_+$ and the dimensionless quantity

$$\tilde\kappa = \gamma_s - \tilde\gamma - (\gamma_1 + \gamma_s)\tilde\epsilon_z. \tag{18}$$

The amplitude of the energy splitting is set by the characteristic angular momentum quantization energy $\hbar\omega_\varphi = \hbar^2\gamma_1/mR^2 \approx 10 \times (10\,\text{nm}/R)^2\,\text{meV}$, but it is reduced by the strain-dependent SOI $v_\varphi mR/\hbar\gamma_1 = 3\tilde\kappa/2\gamma_1$, which in the parameter range considered ranges from about 0.5 at $\epsilon_z = 0$ to about 0.15 at $\epsilon_z = 0.5\epsilon_r$; see Fig. 3. Importantly, the longitudinal strain ϵ_z *decreases* the subband gap Δ. This trend is in contrast to Ge/Si core-shell nanowires, where the strain ϵ_z induced by the Si shell *increases* the energy gap at $p_z = 0$, resulting in a gap $\Delta_{c/s} \approx 0.5\epsilon_z \sim 10$ meV [17–19,47].

To define spin qubits, a subband energy gap Δ in the millielectron volt range is convenient because it reduces the leakage outside of the computational subspace. In strongly strained thin Ge CQWs, this requirement would constrain the maximal values of the radius R to 10–20 nm. While technologically feasible, this requirement can also be relaxed by including an external electric field E_x, e.g., produced by a back or top gate. This field breaks the rotational symmetry and yields the additional energy

$$H_E = -eE_xR\cos(\varphi), \tag{19}$$

which introduces matrix elements with amplitude $eE_xR/2$, coupling eigenstates of the total angular momentum quantum number l to states with $l \pm 1$.

As shown in Fig. 4(b), the effective Hamiltonian $H_{\rm GS} + H_E$ nicely reproduces the energy dispersion of the low-energy states even in the presence of rather large electric fields. As anticipated, E_x also induces a large energy splitting between the ground state and the first excited state at $p_z = 0$. At large values of E_x, the angular coordinate φ is pinned in the vicinity of $\varphi = 0$ and thus the wave function is confined at the top of the well. In this case, one can expand H_E close to $\varphi = 0$, resulting in

$$H_{\rm GS}(p_z = 0) + H_E \approx \frac{p_\varphi^2}{2m_\varphi R^2} + \frac{eE_xR}{2}\varphi^2 + \Delta p_\varphi\sigma_x. \tag{20}$$

Because the mass $m_\varphi \approx 0.06m$ is to good approximation independent of strain, see Fig. 3, the harmonic confinement frequency

$$\omega_E = \sqrt{\frac{eE_x}{m_\varphi R}} \tag{21}$$

is independent of strain and dominates over the smaller gap Δ. In this case, the subband gap between the ground and first excited doublets is to good approximation $\hbar\omega_E \approx 8$ meV at $E_x = 1$ V/μm and $R = 20$ nm, and it decreases slowly $\propto R^{-1/2}$ compared to the faster R^{-2} decay of Δ. To facilitate the comparison to Fig. 4(b), we note that the ratio $\hbar\omega_E/\epsilon_c = \tau/\pi R\sqrt{eE_xR/\epsilon_c}\sqrt{m/\gamma_1 m_\varphi} \approx 0.17$ at $\tau = R/2$ and $eE_xR = \epsilon_c$, in good agreement with the figure.

We also remark that the electric field E_x originates from a gate that breaks rotational symmetry. In contrast, gates

completely wrapped around the CQW produce a radial electric field E_r that generates a *cubic* SOI term

$$H_r = \frac{-4\tilde{\gamma}\gamma_s e E_r \tau}{\pi^4(\gamma_1-2\gamma_s)(2\gamma_s+\gamma_1(2\epsilon_r+\epsilon_z)/\epsilon_c)}\frac{p_-^3\tau^3}{\hbar^3}\sigma_+ + \text{H.c.}, \tag{22}$$

in analogy to planar Ge heterostructures [20,40,55]. While this term can be significant at large values of R, this contribution is negligible in the regime of parameters studied in this work.

Finally, we introduce the magnetic field $\mathbf{B}$ in the effective theory. By writing the Hamiltonian $H_{\mathbf{B}}$ in the radial basis in Eq. (11), and with a second-order Schrieffer-Wolff transformation, we find that, to linear order in $\mathbf{B}$,

$$\begin{aligned}\frac{H_B}{3\kappa\mu_B} = {} & B_x\left\{\cos(\varphi)\left[\left(1-\frac{\tilde{\gamma}}{\kappa}\right)\sigma_z - \frac{\tilde{\kappa}}{\kappa}\frac{z}{R}\sigma_x\right] + \tilde{\epsilon}_z\sin(\varphi)\sigma_y\right\} \\ & + B_y\left\{\sin(\varphi)\left[\left(1-\frac{\tilde{\gamma}}{\kappa}\right)\sigma_z - \frac{\tilde{\kappa}}{\kappa}\frac{z}{R}\sigma_x\right] - \tilde{\epsilon}_z\cos(\varphi)\sigma_y\right\} \\ & + B_z\left[\left(\tilde{\epsilon}_z+\frac{1}{2}\frac{\tilde{\kappa}}{\kappa}\right)\sigma_x + \frac{1}{3\kappa}\frac{m}{m_\varphi}p_\varphi\right].\end{aligned} \tag{23}$$

We omit the negligible spin-independent shift of the dot $-2\mu_B z\{p_\varphi, [B_x\cos(\varphi)+B_y\sin(\varphi)]\}/m_\varphi R$. We emphasize that the magnetic interactions have an angular dependence caused by the transformation U and that the origin of the coordinate system coincides with the center of mass of the quantum dot. In addition, the corrections to the Zeeman energy caused by the high-energy holes are discussed in detail in Appendix C; see, in particular, Eq. (C3).

IV. SPIN QUBITS IN SHORT QUANTUM DOTS

We now study the properties of a spin qubit confined in a quantum dot in the thin CQWs sketched in Fig. 1. The behavior of the spin qubit strongly depends on the length l_z of the dot. We examine two different qubit designs where the dot is long and short compared to the radius R, i.e., $l_z \gg R$ and $l_z \lesssim R$, respectively. Both these regimes can be described by the effective theory introduced in Sec. III. At first, we restrict ourselves to the analysis of the annular CQW shown in Fig. 1(a) and described by the isotropic LK Hamiltonian in Eq. (2). We then show that our theory also well describes the planar CQW in Fig. 1(b). Moreover, our theory models a wide range of devices with general cross sections and is valid even when cubic anisotropies of the LK Hamiltonian are included. A detailed analysis of anisotropic corrections, including results obtained for quantum wells grown along a main crystallographic axis and with square cross sections, is given in Appendix D.

The dynamics of a spin qubit can be mapped to the effective quantum dot Hamiltonian [60–64]

$$H_{\text{QD}} = \frac{\mu_B}{2}\boldsymbol{\sigma}\cdot\left(\underline{g} - \sum_{i=x,y,z}\frac{eE_i(t)R}{\hbar\omega_\varphi}\delta\underline{g}^i\right)\mathbf{B}, \tag{24}$$

parametrized by a tensor $\underline{g}$ of g-factors and a tensor $\delta\underline{g}^i$ driving spin transitions via the ac field $E_i(t)$.

An accurate model to describe short quantum dots, with $l_z \lesssim R$, is provided by the Hamiltonian

$$\begin{aligned}H_{\text{SD}} = {} & \frac{\hbar\bar{\omega}_\varphi}{2}p_\varphi^2 + \Delta p_\varphi\sigma_x - \frac{\hbar\bar{\omega}_z}{2}\lambda_z + \frac{\hbar v_z}{\sqrt{2}\bar{l}_z}\lambda_y\sigma_y \\ & - eE_xR\cos(\varphi),\end{aligned} \tag{25}$$

obtained by projecting Eqs. (12) and (19) onto the first two eigenstates of the longitudinal confinement, energetically separated by $\hbar\bar{\omega}_z \propto 1/\bar{l}_z^2$. We introduce the longitudinal mass $m_z = (1/m^* + 1/\delta m)^{-1} \approx 0.06m$ and SOI velocity $v_z = v_- + v_+ \approx 6.5\,\hbar/mR$; see Eqs. (13) and Fig. 3. Strain weakly affects these parameters and in the regimes studied it results in variations of $\lesssim 15\%$ from the numerical values provided here. We also introduce the exact longitudinal and angular frequencies $\bar{\omega}_z = \omega_z\sqrt{m/\gamma_1 m_z}$ and $\bar{\omega}_\varphi = \omega_\varphi\sqrt{m/\gamma_1 m_\varphi}$, which include the small corrections of longitudinal and angular masses from the average value m/γ_1; in analogy, we define the exact harmonic length $\bar{l}_z = l_z(\gamma_1 m_z/m)^{1/4}$. Here, the Pauli matrices $\lambda_{x,y,z}$ act on these orbital states, while $\sigma_{x,y,z}$ act on the pseudospin. We remark that p_φ is the total angular momentum, and that at $E_x = 0$ the degenerate Kramers partners are the eigenstates of $p_\varphi\sigma_x$ (and not of σ_x) to the same eigenvalue; see Eq. (15).

To proceed further, it is convenient to eliminate the term $\propto \lambda_y\sigma_y$ by the rotation $H_{\text{SD}} \to e^{i\theta_z\lambda_x\sigma_y/2}H_{\text{SD}}e^{-i\theta_z\lambda_x\sigma_y/2}$, where $\theta_z = \arctan(\sqrt{2}v_z/\bar{\omega}_z\bar{l}_z)$. After this transformation, the low-energy Hamiltonian acting on the ground-state Kramers partners is

$$H_{\text{SD}}^{\text{GS}} = \frac{\hbar\bar{\omega}_\varphi}{2}p_\varphi^2 + \Delta\cos(\theta_z)p_\varphi\sigma_x - eE_xR\cos(\varphi). \tag{26}$$

At weak electric fields, the subband gap that energetically separates the spin qubit to the noncomputational subspace is

$$E_g = \sqrt{\Delta^2\cos(\theta_z)^2 + e^2E_x^2R^2}. \tag{27}$$

In quantum wells with $R = 20$ nm, the gap is $E_g \approx 1$ meV at $E_x = 0$ and it increases with E_x. At large values of

$E_x \gtrsim 1$ V/μm, the energy gap approaches $\hbar\omega_E \gtrsim 8$ meV; see Eq. (21). Also, in this basis, Eq. (23) reduces to

$$H^B_{\rm SD} = 3\kappa\mu_B B_z\left[\left(\tilde{\epsilon}_z + \frac{1}{2}\frac{\tilde{\kappa}}{\kappa}\right)\cos(\theta_z)\sigma_x + \frac{1}{3\kappa}\frac{m}{m_\varphi}p_\varphi\right] + 3\kappa\mu_B[B_x\cos(\varphi) + B_y\sin(\varphi)]q_0\sigma_z + 3\kappa\mu_B[B_x\sin(\varphi) - B_y\cos(\varphi)]\tilde{\epsilon}_z\sigma_y, \quad (28)$$

where we introduce the size-dependent quantity

$$q_0 = \left(1 - \frac{\tilde{\gamma}}{\kappa}\right)\cos(\theta_z) - \frac{\tilde{\kappa}}{\kappa}\frac{\bar{l}_z}{\sqrt{2}R}\sin(\theta_z). \quad (29)$$

A. Defining the spin qubit

We now discuss the matrix $\underline{g}$ of g-factors that determines the energy gap of different spin states in the quantum dot. From Eqs. (26) and (28), $\underline{g}$ can be derived by projecting $H^B_{\rm SD}$ onto the degenerate ground state of $H^{\rm GS}_{\rm SD}$. The resulting g-tensor is diagonal and $\underline{g} = g_{ii}\delta_{ij}$. The diagonal elements g_{ii} are shown in Fig. 5. We note that the effective theory in Eq. (25) is reasonably accurate and approximates well a numerical simulation of a three-dimensional quantum dot obtained from Eq. (1). In Fig. 5(a), we show the dependence of g_{ii} on the size of the dot at $E_x = 0$. In this case, the eigenstates of Eq. (26) coincide with the eigenstates of $p_\varphi\sigma_x$ given in Eq. (15) and one obtains $g_{xx} = -g_{yy} = -3\kappa(q_0 - \tilde{\epsilon}_z)$ and $g_{zz} = 6\kappa(\tilde{\epsilon}_z + \tilde{\kappa}/2\kappa)\cos(\theta_z) - m/m_\varphi$.

Because of the orbital magnetic field, g_{zz} is rather large, and only weakly dependent on the length l_z of the dot. A similar enhancement of the effective Zeeman energy emerges in topological insulator nanowires [42], where the leading contribution is the SOI-induced term $\propto \tilde{\kappa}$. Because in competing hole-based architectures, such as Ge/Si core-shell nanowires, $g_{zz} \sim 1$ is rather small [65], the large value of g_{zz} in thin CQWs is particularly advantageous for topological quantum computing in seeking exotic particles, such as Majorana bound states [45,66].

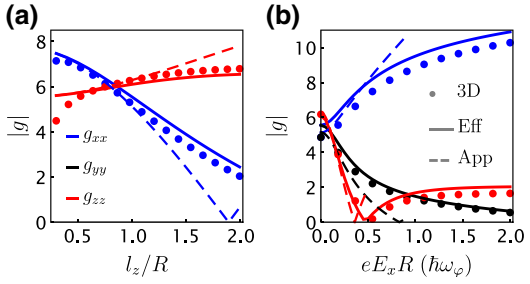

FIG. 5. Matrix of g-factors of a hole spin qubit in a thin Ge CQW. We show the diagonal elements g_{xx}, g_{yy}, g_{zz} in blue, black, and red, respectively; the off-diagonal elements are zero. We compare the results of a numerical simulation of a three-dimensional (3D) quantum dot obtained by discretizing Hamiltonian (1) with an annular cross section (circles), against the effective theory (25) (solid lines) and the approximate formulas in Eqs. (30) (dashed lines). In (a), we show g_{ii} as a function of the length l_z of the quantum dot at $E_x = 0$; in this case, $|g_{xx}| = |g_{yy}|$. In (b), we show g_{ii} as a function of the electric field E_x at $l_z = R$. In both cases, we consider $\epsilon_r = 3\epsilon_z = \epsilon_c$ and $\tau = R/2$. At $R = 20$ nm, the electric field is $E_x \in [0, 0.26]$ V/μm.

At small values of E_x, one can still use a few eigenstates in Eq. (15). By using the energetically lowest two quasidegenerate Kramers partners and by introducing the E_x-dependent angle $\theta_E = \arctan[eE_xR/\Delta\cos(\theta_z)]$, to second order in perturbation theory, one finds that

$$g_{xx} = 3\kappa\left[\tilde{\epsilon}_z\cos(\theta_E) - q_0 - q_0\frac{m_\varphi}{m}eE_xR\sin(\theta_E)\right], \quad (30a)$$

$$g_{yy} = 3\kappa\left[q_0\cos(\theta_E) - \tilde{\epsilon}_z - \tilde{\epsilon}_z\frac{m_\varphi}{m}eE_xR\sin(\theta_E)\right], \quad (30b)$$

$$g_{zz} = 6\kappa\left(\tilde{\epsilon}_z + \frac{\tilde{\kappa}}{2\kappa}\right)\cos(\theta_z) - \frac{m}{m_\varphi}\cos(\theta_E). \quad (30c)$$

These equations qualitatively capture the trend of the g-factors as a function of E_x, but they are not quantitatively accurate at large values of E_x, as shown in Fig. 5(b).

At large values of E_x, Eq. (26) is approximated by a harmonic oscillator with harmonic frequency ω_E [see Eqs. (20) and (21)], resulting in $g_{xx} = -6\kappa\, e^{-\varphi_E^2(\varphi_S^{-2}+1/4)}[q_0\cosh(\varphi_E^2/\varphi_S) - \tilde{\epsilon}_z\sinh(\varphi_E^2/\varphi_S)]$, $g_{yy} = 6\kappa\, e^{-\varphi_E^2(\varphi_S^{-2}+1/4)}[q_0\sinh(\varphi_E^2/\varphi_S) - \tilde{\epsilon}_z\cosh(\varphi_E^2/\varphi_S)]$, and $g_{zz} = 6\kappa\tilde{\epsilon}_z\cos(\theta_z)$ with angular width $\varphi_E = \sqrt{\omega_\varphi m/\gamma_1 m_\varphi\omega_E}$ and SOI angle $\varphi_S^{-1} = m_\varphi v_\varphi\cos(\theta_z)R/\hbar$ [67]. Because, depending on the amplitude of the longitudinal strain ϵ_z, the limiting values of the g-factor for $E_x = 0$ and $E_x \to \infty$ can have opposite signs, there could be points at finite values of E_x where the g_{ii} vanish, as shown in Fig. 5(b).

We note that the g-tensor is strongly anisotropic and that it is tunable by the electric field and by designing the strain, especially via the outer shell thickness. This behavior is typical of hole nanostructures [12,68–72]. In contrast to Ge/Si core-shell nanowires [14,69], however, in a thin CQW the g-factor is only strongly modulated at weak values of the electric field E_x, and at $E_x \gtrsim 1$ V/μm, g becomes weakly dependent of E_x. In particular, g is *independent* of E_x when **B** is aligned to the quantum well and it only varies as $E_x^{-1/2}$ when **B** is perpendicular to it. This property suggests that spin qubits in these devices can have a low susceptibility to charge noise, enabling long coherence times.

B. Decoherence of the qubit

We now discuss the coherence time of these hole spin qubits. We focus on the dephasing of the qubits caused by charge noise, the leading decoherence mechanism in current hole spin qubits. Relaxation processes caused, for

example, by phonons have been discussed in detail in structures with similar SOI [72,73], where at the small values of the magnetic field considered in this work their effect is estimated to be orders of magnitude smaller than typical dephasing times.

We examine a free induction decay experiment, where the spin is prepared in an eigenstate of the Zeeman energy and left idle. In this case, random fluctuations of the electric potential result in charge noise with a typical $1/f$ spectral function $S(\omega) = \langle \delta V^2 \rangle / |\omega|$. Although these fluctuations can have different microscopic origins, including disorder-induced two-level systems or gate noise, their effect on the qubit coherence time uniquely depends on $S(\omega)$ and on the qubit sensitivity to variations of the electrostatic potential [74], and we model them as if they were caused by fluctuation of gate potentials [75]. We consider here magnetic fields aligned to the main confinement axes $i = (x, y, z)$. Because of the dependence of g on the external electric field, charge noise causes dephasing with decay rate [20,39,76]

$$\frac{1}{(T_2^*)_i} \approx \frac{\omega_Q^i}{\sqrt{2\pi}} \frac{1}{g_{ii}} \frac{\partial g_{ii}}{\partial V} \sqrt{\langle \delta V^2 \rangle}. \tag{31}$$

We neglect small logarithmic corrections caused by the divergence of the spectral function at low frequency [76], and we assume that the noise is Gaussian [77]. The qubit frequency $\omega_Q^i = g_{ii} \mu_B B_i / \hbar$ depends on the external magnetic and electric fields and we restrict our analysis to microwave frequencies $\omega_Q^i / 2\pi \sim$ 1–20 GHz.

An estimate of the sensitivity of the g-factor to the potential fluctuations can be obtained by considering how g is modified by a small random fluctuating electric field $\mathbf{E}(t)$. When a strong dc field E_x is applied by the gates and B is aligned to the main confinement axes i, the main contribution to dephasing comes from the fluctuations of E_x. These fluctuations yield a contribution to the Hamiltonian $\propto \sigma_i E_x(t) \delta g_{ii}^x B_i$ that is aligned to the Zeeman energy $\omega_Q^i \sigma_i / 2$ and directly leads to dephasing. In contrast, we anticipate that small time-dependent fluctuations of $E_{y,z}$ yield contributions $\propto \sigma_{j \neq i} E_{y,z}(t) B_i$ that lead to spin flips and to relaxation; see Eqs. (32). Because the spectral function of charge noise has significantly more weight at low frequencies and it decays at high frequencies, the relaxation rates $\propto S(\omega_Q^i) = \langle \delta V^2 \rangle / \omega_Q^i$ [76] are much smaller than the dephasing rates in Eq. (31) and we neglect them here. Moreover, to connect the fluctuation of the electric field to the measurable fluctuations of the chemical potential of the dot, we assume that the noise comes from the electrodes, such that $\partial g_{ii} / \partial V \approx \alpha \delta g_{ii}^x / \hbar \omega_\varphi$; see Eq. (24). Here, $\alpha \sim 0.1$–0.5 is the lever arm of the gate [78], whose precise value depends on the device design, resulting in the typical values $\sqrt{\langle \delta \mu^2 \rangle} \approx \alpha \sqrt{\langle \delta V^2 \rangle} \sim 0.1$–$10$ μeV [75,79].

In Fig. 6, we show the decay time T_2^* of a typical hole spin qubit in a thin CQW as a function of the applied

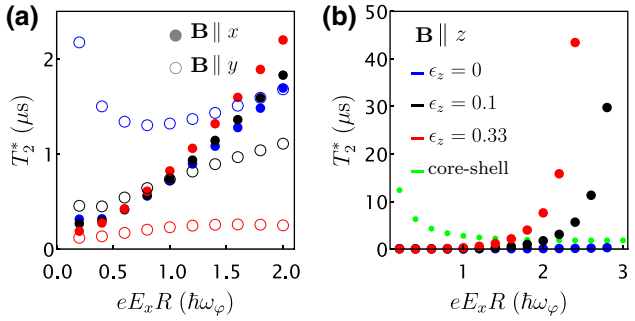

FIG. 6. Dephasing time T_2^* of a hole spin qubit in a thin CQW as a function of electric field E_x. In (a), we show with filled and open circles the time T_2^* when the magnetic field is aligned to the x and y directions, respectively; in (b), we show the result when $\mathbf{B} \parallel z$. Blue, black, and red circles indicate longitudinal strain $\epsilon_z = 0$, $\epsilon_z = \epsilon_c/10$, and $\epsilon_z = \epsilon_c/3$, respectively. For the simulation, we consider a free induction decay experiment, in a qubit with frequency $\omega_Q^i / 2\pi = 5$ GHz and $\alpha \sqrt{\delta V^2} = 1$ μeV. We also use $R = l_z = \tau/2 = 20$ nm and $\epsilon_r = \epsilon_c$. The green circles in (b) show T_2^* of a hole spin qubit in a Ge/Si core-shell nanowire with $\epsilon_z = \pi^2 \hbar \omega_\varphi / 4$ and $R = l_z = 20$ nm.

electric field. When the magnetic field is applied in the (x, y) plane, the estimated values of T_2^* are in the 100-ns range, and their precise values depend on E_x and on the strain ϵ_z. In particular, when $\mathbf{B} \parallel E_x$, the strain dependence of T_2^* is to good approximation negligible and T_2^* increases monotonically with E_x. In contrast, when $\mathbf{B} \parallel y$, the electric field dependence is weaker, and T_2^* is strongly affected by ϵ_z. The decrease in T_2^* as strain increases originates from the reduced value of g_{yy} at large ϵ_z and large E_x; see Eq. (31). For example, at $\epsilon_z = 0.33 \epsilon_c$ and $E_x = \hbar \omega_\varphi / eR \approx 0.13$ V/μm at $R = 20$ nm, one finds that $T_2^* \approx 225$ ns for the parameters considered. This dephasing time can be further improved by echo sequences [80,81]. We emphasize that the results in Fig. 6 are estimations of the effect of charge noise obtained by using $1/f$ spectral functions with $\sqrt{\langle \delta \mu^2 \rangle} = 1$ μeV, a value which, while optimistic for current Ge/Si core-shell nanowires [14], is realistic for many other semiconductor nanostructures [75], and thus we believe is within reach in future CQWs.

Strikingly, the flatness of the g-factor in the z direction as a function of E_x results in a rather long coherence time of qubits in strained CQWs, with an enhanced value of T_2^* when $E_x \gtrsim 2\hbar\omega_\varphi / eR \approx 0.26$ V/μm at $R = 20$ nm. This trend appears in CQWs and does not occur in Ge/Si core-shell nanowires; see Fig. 6(b). At low values of ϵ_z, the small value of $g_{zz} \propto \tilde{\epsilon}_z$ at large E_x reduces T_2^*. Because g_{zz} is only weakly dependent on the quantum dot length l_z [see Fig. 5(a)], this enhancement also occurs in long quantum dots. We emphasize that, in contrast to alternative proposals where the lifetime of the qubit is enhanced only at fine-tuned sweet spots [39–41], in thin Ge CQWs the qubit is to good approximation insensitive to charge

noise in a wide range of E_x, thus enabling highly coherent qubits with a low sensitivity to charge noise, a major issue in state-of-the-art hole spin quantum processors [14].

C. Driving the qubit

We now discuss two qualitatively different mechanisms to drive the hole spin qubit. First, we note that in short quantum dots, where $l_z \lesssim R$, shaking the hole wave function along the quantum well [82] does not result in ultrafast Rabi oscillations. As discussed in Sec. V, this mechanism is more convenient in long quantum dots because the Rabi frequency $\omega_R \propto l_z^4$ [20]; see Eq. (38). However, as shown in Fig. 4(b), in a CQW the electric field E_x confines the hole to the top of the cross section and thus fast Rabi oscillations are enabled when the hole is periodically driven in the angular direction by an ac field $E_y(t) = E_y^{\rm ac}\sin(\omega_D t)$, perpendicular to the dc field E_x. In particular, $E_y(t)$ shakes the wave function along a weak confinement direction and because of the large SOI in these systems, this motion results in spin flips, in analogy to electric dipole spin resonance (EDSR) [82].

These spin transitions are parametrized by the matrix δg^y of effective g-tensors [see Eq. (24)], and are the fastest when the dc field E_x is comparable to the SOI gap Δ; for this reason, we restrict ourselves to the analysis of the moderately weak electric fields. By including the small potential $-eE_y(t)R\sin(\varphi)$ in Eq. (26) and by using second-order perturbation theory, we find that the driving term is $\propto E_y(t)(\sigma_x \delta g^y_{xy} B_y + \sigma_y \delta g^y_{yx} B_x)$ with

$$\delta g^y_{xy} = 3\kappa\sin(\theta_E)\left[\frac{\hbar\omega_\varphi}{E_g}q_0 + \frac{m_\varphi\gamma_1}{m}(q_0 + \tilde{\epsilon}_z\cos(\theta_E))\right], \tag{32a}$$

$$\delta g^y_{yx} = 3\kappa\sin(\theta_E)\left[\frac{\hbar\omega_\varphi}{E_g}\tilde{\epsilon}_z + \frac{m_\varphi\gamma_1}{m}(\tilde{\epsilon}_z + q_0\cos(\theta_E))\right]. \tag{32b}$$

For completeness, we also note that a small electric field $E_z(t)$ applied parallel to the CQWs produces a driving term $\propto E_z(t)(\sigma_z\delta g^z_{zx}B_x + \sigma_x\delta g^z_{xz}B_z)\omega_\varphi/\tilde{\omega}_z$.

Here we focus on the effect of E_y and we show the terms δg^y_{ij} in Fig. 7. In particular, we highlight their dependence on E_x and on the longitudinal strain ϵ_z that can be designed by the thickness of the outer Si shell; see Eqs. (5). We note that at small values of E_x, Eqs. (32) approximate well the driving δg^y_{xy} when $\mathbf{B} \parallel y$, but are quantitatively inaccurate for δg^y_{yx} when $\mathbf{B} \parallel x$, especially at small ϵ_z. The latter term is generally smaller and, thus, to enhance the Rabi frequency, it is convenient to align $\mathbf{B}$ to the ac drive. Moreover, ϵ_z strongly speeds up the driving, in sharp contrast to elongated dots in Ge/Si core-shell nanowires, where the Rabi frequency at small electric fields is $\propto 1/\epsilon_z$ [17–19]. We also note that, while in principle a similar driving mechanism can also occur in core-shell nanowires, in the parameter range considered, the terms δg^y_{ij} are negligible there. When $\mathbf{B} \parallel z$, this effect vanishes.

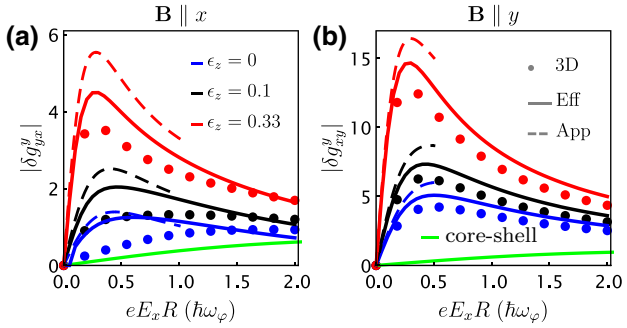

FIG. 7. Driving of a hole spin qubit in a thin Ge CQW by an ac electric field $E_y(t)$. In (a) and (b), we show the nonzero elements δg^y_{yx} and δg^y_{xy} of the matrix δg^y as a function of the dc electric field E_x; see Eq. (24). With blue, black, and red curves, we show different values of longitudinal strain $\epsilon_z = 0$, $\epsilon_z = \epsilon_r/10$, and $\epsilon_z = \epsilon_r/3$, respectively. We use $\tau = R/2$, $l_z = R$, and $\epsilon_r = \epsilon_c$. The circles and the solid and dashed lines represent results obtained by Eqs. (1), (25), and (32), respectively. For the solid and dashed lines, we use the two lowest Kramers partners at $E_x = 0$. The green lines show the results obtained by simulating a Ge/Si core-shell nanowire with $\epsilon_z = \pi^2\hbar\omega_\varphi/4$, where this effect is negligible.

We now estimate the frequency ω_R of the Rabi oscillations generated by these driving terms when $\mathbf{B}$ is aligned to the $i = \{x, y\}$ directions. In this case, the spin states are split by $\hbar\omega^i_Q = g_{ii}\mu_B B_i$, and when the qubit is in resonance with the drive, i.e., $\omega_D = \omega^i_Q$, we find that

$$\frac{\omega^i_R}{2\pi} = \frac{\omega_D}{2\pi}\frac{eE_y^{\rm ac}R}{2\hbar\omega_\varphi}\frac{\delta g^y_{ji}}{g_{ii}} \approx 0.2\ \text{GHz} \times \frac{\delta g^y_{ji}}{g_{ii}}. \tag{33}$$

Here, we define the index $j \neq i$, for example $\omega^x_R \propto \delta g^y_{yx}/g_{xx}$. The numerical prefactor is obtained by considering a CQW with radius $R = 20$ nm, such that $\hbar\omega_\varphi = 2.5$ meV, and for the typical experimental values $\omega_D/2\pi = 5$ GHz and $E_y^{\rm ac} = 10\ \text{mV}/\mu\text{m}$ [14]. For thicker quantum wells, this factor increases as R^3, but the energy gap at $E_x = 0$ also decreases as $1/R^2$. By comparing Figs. 5 and 7, we also observe that $\delta g^y_{yx} \lesssim g_{xx}$ when $\mathbf{B} \parallel x$, and $\delta g^y_{xy} \gtrsim g_{yy}$ when $\mathbf{B} \parallel y$. For example, in a strongly strained device with a thick outer shell, at $E_x = \hbar\omega_\varphi/eR \approx 0.13\ \text{V}/\mu\text{m}$ and $R = 20$ nm, one obtains $\delta g^y_{xy}/g_{yy} \approx 6$, resulting in $\omega^y_R/2\pi \approx 1.2$ GHz, thus enabling ultrafast qubit operations at low power. At this value of E_x, we also find that $g_{yy} = 1.35$, such that $\omega^y_B/2\pi = 5$ GHz at $B = 0.25$ T, and the subband energy gap is $E_g = 2.3$ meV.

In addition, the g-factor can also be modulated by an ac field $E_x(t) = E_x^{\rm ac}\cos(\omega_D t)$ applied in the x direction,

resulting in the variation $\delta\underline{g}^x$ of the g-factors in Eqs. (30):

$$\frac{\delta g^x_{xx}}{3\kappa\sin(\theta_E)} = \frac{\hbar\omega_\varphi}{E_g}\tilde{\epsilon}_z\cos(\theta_E) + \frac{m_\varphi\gamma_1}{2m}(3+\cos(2\theta_E))q_0, \tag{34a}$$

$$\frac{\delta g^x_{yy}}{3\kappa\sin(\theta_E)} = \frac{\hbar\omega_\varphi}{E_g}q_0\cos(\theta_E) + \frac{m_\varphi\gamma_1}{2m}(3+\cos(2\theta_E))\tilde{\epsilon}_z, \tag{34b}$$

$$\delta g^x_{zz} = \frac{m}{2m_\varphi}\frac{\hbar\omega_\varphi}{E_g}\sin(2\theta_E). \tag{34c}$$

When the magnetic field is aligned to the x, y, z directions, these terms are aligned to the Zeeman vector (i.e., the spin quantization axis $\propto \underline{g}\mathbf{B}$) and thus they do not induce spin transitions, and only modulate the qubit energy. However, at arbitrary orientations of $\mathbf{B}$, because of the tunable anisotropy of the g-factor, some driving terms are perpendicular to the Zeeman vector, and those terms can yield Rabi oscillations via the so-called g-tensor modulation [60–64]. In particular, when the qubit energy $\hbar\omega_B = \mu_B\sqrt{g^2_{xx}B^2_x + g^2_{yy}B^2_y + g^2_{zz}B^2_z}$ is at resonance with ω_D, the Rabi frequency induced by $E^{\rm ac}_x$ is

$$\frac{\omega_R}{2\pi} = \frac{\omega_D}{2\pi}\frac{eE^{\rm ac}_x R}{2\hbar\omega_\varphi}\left|\frac{\delta\underline{g}^x\cdot\mathbf{B}}{\hbar\omega_B/\mu_B} - \frac{(\delta\underline{g}^x\cdot\mathbf{B})\cdot(\underline{g}\cdot\mathbf{B})}{\hbar^3\omega_B^3/\mu_B^3}(\underline{g}\cdot\mathbf{B})\right|. \tag{35}$$

In Fig. 8, we analyze the dependence of this driving mechanism on the direction of the magnetic field for different values of the dc field E_x. We consider here an arbitrary field $\mathbf{B} = B(\cos(\theta_B)\sin(\varphi_B), \cos(\theta_B)\cos(\varphi_B), \sin(\theta_B))$; see Fig. 1. We observe that $\omega_R = 0$ when $\mathbf{B}$ is aligned to a confinement axis, but in certain parameter regimes it becomes comparable to the values obtained by driving $E^{\rm ac}_y$. Comparing Fig. 8(a) to Fig. 5, we note that, when $\mathbf{B}$ is slightly misaligned from the z direction, a large ω_R can be reached close to the value of E_x where g_{zz} vanishes, in particular, at $E_x = 0.4\hbar\omega_\varphi/eR$, $g_{zz}\approx 1$. Away from these sweet spots in both electric field and magnetic field directions, ω_R is strongly reduced, and the optimal direction of $\mathbf{B}$ changes; see Fig. 8(b). In contrast, when the qubit is driven by $E^{\rm ac}_y$, the optimal values of ω_R occur at the fixed direction $\mathbf{B}\parallel y$ and persist in a wide range of E_x. For this reason, the $E^{\rm ac}_y$ driving is more convenient in experiments comprising chains of quantum dots in the CQW subjected to a global fixed $\mathbf{B}$ field, and we focus on it in the following.

Finally, we remark that the decay of Rabi oscillations in time is characterized by a time scale $T_2^{\rm Rabi}$ that, for hole spin qubits, is typically orders of magnitude larger than the dephasing time T_2^* of idle qubits [7,14] and depends on the details of the spectral function of the noise at higher frequencies and on the microscopic driving mechanism of the

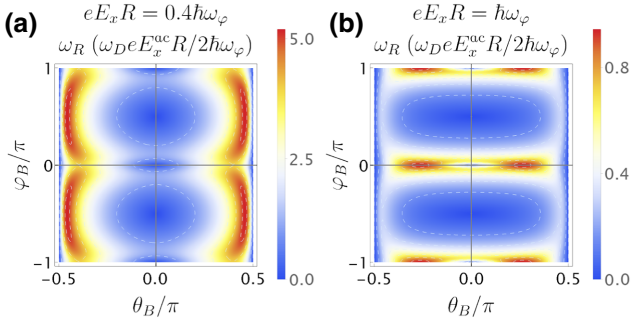

FIG. 8. Driving of a hole spin qubit in a thin Ge CQW by g-tensor modulation via an ac electric field $E^{\rm ac}_x$. In (a) and (b), we show the Rabi frequency as a function of the direction of the applied magnetic field for two different values of the dc field E_x. The results shown here use Eq. (35) with parameters obtained by discretizing Hamiltonian (1). The prefactor of ω_R is 200 MHz in typical dots; see Eq. (33).

Rabi oscillations. While a detailed analysis of the dependence of $T_2^{\rm Rabi}$ in hole nanostructures on these factors is a relevant question for scaling up hole spin qubits, in this work we restrict ourselves to the analysis of T_2^*.

D. Planar Ge curved quantum wells

Similar qubits can also be designed in planar systems, providing a technologically competitive and scalable architecture for hole-based quantum computers. A possible example of a planar CQW is sketched in Fig. 1(b) and can be manufactured by growing a Ge quantum well over a Si substrate. Because the spin qubit proposed in Sec. IV works well at $E_x \approx \hbar\omega_\varphi/eR$, where the hole wave function is confined to the top half of the shell [see Fig. 4(b)], we expect an analogous behavior in a spin qubit defined in planar CQWs.

In Fig. 9, we show the results of a numerical simulation of the Hamiltonian (1) defined in the planar CQW sketched in Fig. 1(b). In Fig. 9(a), we show the g-factor of a quantum dot of length $l_z = R$ as a function of the electric field E_x perpendicular to the substrate. We observe that, when the magnetic field is perpendicular to the well, there is a critical electric field above which the behaviors of g_{xx} and g_{yy} as a function of E_x resemble those shown in Fig. 5(b). The position of this critical electric field depends on the longitudinal strain ϵ_z and is shifted to more negative values as ϵ_z increases. Moreover, in analogy to annular CQWs, g_{zz} is a rather flat function of E_x and it increases with ϵ_z, approaching the high field limiting value $g_{zz}\approx 6\kappa\tilde{\epsilon}_z\cos(\theta_z)$. These results indicate that qubits in planar CQWs can be as insensitive to charge noise as qubits in annular CQWs.

In analogy to Fig. 7(b), we also find that these qubits can be driven fast by an ac electric field $E_y(t)$ applied parallel to the substrate. In particular, we observe that the

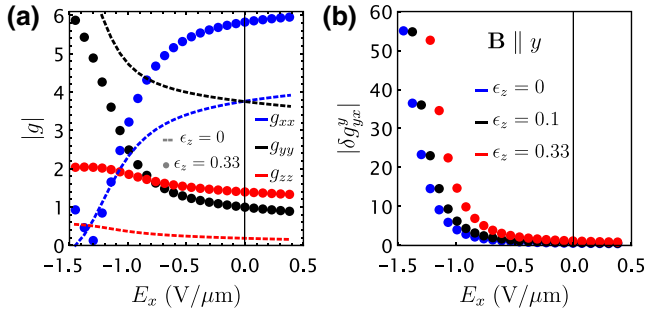

FIG. 9. Hole spin qubit in a planar thin shell quantum dot. In (a) we show the $|g|$-factor as a function of the electric field applied perpendicular to the substrate and in (b) we show the driving term δg^y_{yx}, obtained by an ac field $E_y(t)$ aligned to the magnetic field **B**. For typical experimental parameters, the Rabi frequency is $\omega_R/2\pi \approx 200$ MHz $\times\, \delta g^y_{yx}/g_{yy}$. For the plots, we consider $l_z = R = \tau/2 = 20$ nm [see Fig. 1(b)] and $\epsilon_r = \epsilon_c$. Dashed lines in (a) refer to $\epsilon_z = 0$, while points are evaluated at $\epsilon_z = 0.33\epsilon_c$. In (b) different colors correspond to different strains and the values of ϵ_z are given in units of ϵ_c.

driving strength can easily exceed the gigahertz range and becomes even stronger than in annular CQWs as the dc electric field E_x decreases. At lower values of E_x, however, the subband gap E_g separating computational and noncomputational states also decreases. In the range of parameters examined here $E_g \gtrsim 0.5$ meV.

We note that at $E_x \lesssim -2.5$ V/μm, E_g drops to zero and one obtains two degenerate quantum dots at the two edges of the quantum well. We envision protocols where these two quantum dots can be exchange coupled and used to perform fast readout schemes in analogy to the corner dots in Si FETs [83–85], but we do not investigate these intriguing possibilities here.

V. SPIN QUBITS IN LONG QUANTUM DOTS

When $l_z \gg R$, the longitudinal confinement energy $\hbar\omega_z = \hbar^2\gamma_1/ml_z^2$ is much smaller than the angular momentum quantization energy $\hbar\omega_\varphi$. However, because of longitudinal strain, $\hbar\omega_z$ can still be comparable to the SOI energy Δ, that is, by a factor $3\tilde{\kappa}/2\gamma_1 \sim 0.5$–$0.15$ smaller than $\hbar\omega_\varphi$; see Eq. (17). For this reason, a simple description of the system for moderate electric fields is obtained by projecting the effective theory in Eqs. (12) and (19) onto the low-energy states $|g^{l=1}_{1,2}\rangle$ and $|e^{l=1}_{1,2}\rangle$ in Eq. (15), resulting in the one-dimensional Hamiltonian

$$H_{\rm LD} = \frac{p_z^2}{2m_z} - \frac{\Delta}{2}\lambda_z - \frac{eE_xR}{2}\lambda_x + v_z p_z \lambda_x\sigma_y + \frac{m_z\bar{\omega}_z^2}{2}z^2, \tag{36}$$

where $\lambda_{x,y,z}$ and $\sigma_{x,y,z}$ are Pauli matrices acting on the orbital and pseudospin subspaces, respectively.

In this regime, the Ge CQW mimics a Ge/Si core-shell nanowire, and Eq. (36) is qualitatively analogous to the well-known model discussed in detail in Refs. [17–19,69]. The direct Rashba SOI velocity [19]

$$v = \frac{eE_xR}{\sqrt{\Delta^2 + (eE_xR)^2}}v_z \tag{37}$$

is particularly important for spin qubits. In fact, in EDSR experiments [14,20,82] where an ac field $E_z^{\rm ac}\cos(\omega_D t)$ is applied along the quantum well, and B is perpendicular to the vector of the SOI (here pointing along the y direction [19]), v is directly related to the Rabi frequency ω_R by

$$\frac{\omega_R}{2\pi} = \frac{\omega_D}{2\pi}\frac{veE_z^{\rm ac}}{\hbar\bar{\omega}_z^2}. \tag{38}$$

Moreover, the subband energy gap Δ is renormalized by E_x and by the SOI velocity v_z and it is approximately corrected as

$$\Delta \to E_g \approx e^{-m_z^2v_z^2\bar{l}_z^2/\hbar^2[\Delta^2+(eE_xR)^2]}\sqrt{\Delta^2+(eE_xR)^2}. \tag{39}$$

Equation (37) and the square root in Eq. (39) are obtained by rewriting Eq. (36) in the basis that diagonalizes $H_{\rm LD}$ at $p_z = 0$. The overall Gaussian suppression of the subband gap is most relevant at weak electric field values. It can be derived by first removing the direct couplings between the ground and first excited states by performing a spin and orbital-dependent shift $e^{-im_zv_zz\lambda_x\sigma_y/\hbar\sqrt{\Delta^2+(eE_xR)^2}}$ and then by averaging the resulting potential $\sqrt{\Delta^2+(eE_xR)^2}\cos[2m_zv_zz/\hbar\sqrt{\Delta^2+(eE_xR)^2}]$ over the harmonic oscillator ground state. This correction closely resembles the SOI-induced g-factor renormalization in nanowires with a large SOI [12,18,69,86], and in the short dot case it approaches Eq. (27).

As shown in Fig. 10, the simple approximate Eqs. (37) and (39) give reasonable agreement with a complete three-dimensional simulation of a quantum dot even when the dot is moderately short and $E_g \sim \hbar\bar{\omega}_z$.

There are some noteworthy quantitative differences between CQWs and core-shell nanowires that significantly impact the performance of the spin qubit; these differences are highlighted in Fig. 10. First, as discussed in Sec. III, because of strain the energy gap Δ is much smaller in a CQW than in core-shell nanowires where $\Delta_{c/s} \approx 0.5\epsilon_z \sim 10$ meV. For this reason, in moderately long quantum dots defined in a CQW the energy gap to the first excited doublets is E_g at $E_x = 0$ and it approaches $\hbar\omega_z$ only at finite values of E_x. Moreover, the dipole energy $-eE_xR\lambda_x/2$ in Eq. (36) is 3.3 times larger in a CQW than in a core-shell nanowire, where this term is $-0.15eE_xR\lambda_x$ [18]. The significantly different ratio of dipole energy and subband gap strongly impacts the dependence of the Rabi frequency ω_R on E_x; see Fig. 10(b). In fact, in a CQW the optimal direct

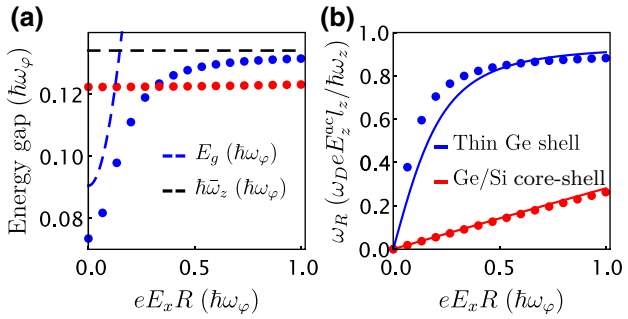

FIG. 10. Electric field dependence of the subband energy gap and Rabi frequency in long quantum dots. We compare thin Ge CQWs (blue) and Ge/Si core-shell nanowires (red). The lines are obtained by the effective theory in Eq. (36). The circles show a numerical simulation of a three-dimensional quantum dot obtained by discretizing Hamiltonian (1) with an annular (cylindrical) cross section, a harmonic potential along z, and with $\epsilon_r = 3\epsilon_z = 3\epsilon_c$ ($\epsilon_z = \pi^2\hbar\omega_\varphi/4$) for the CQW (core-shell nanowire). We use $\tau = R/2$ and $l_z = 3R$. In (a), we show the energy gap between the ground and first excited doublets. The dashed blue line is obtained by Eq. (39) and the dashed black line shows $\bar{\omega}_z$. In (b) we show the Rabi frequency ω_R at resonance; see Eqs. (37) and (38). For realistic experimental parameters $\omega_D/2\pi = 5$ GHz, $E_z^{ac} = 10$ mV/μm, $l_z = 30$ nm, and $\hbar\omega_z = 1.1$ meV, the prefactor of the Rabi frequency is $\omega_D eE_z^{ac} l_z/\hbar\omega_z \approx 1.4$ GHz. For the Ge/Si core-shell nanowire, we use the mass $m_z = 0.06m$ and the SOI velocity $v = 2 \times 0.15 \times 6.5eE_xR/\Delta_{c/s}$, with gap $\Delta_{c/s} = 0.5\epsilon_z$.

Rashba SOI is obtained at values of E_x that are about 10 times smaller than in core-shell nanowires, and v remains constant over a wide range of E_x, enabling ultrafast qubit operations at low power even at small E_x.

We also remark that, as discussed in Sec. IV B, in a strained CQW at sufficiently large E_x, when the magnetic field is applied along the quantum well, the g-factor is to good approximation independent of E_x, suppressing the sensitivity of the spin to charge noise and significantly boosting the coherence time and fidelity of these qubits.

VI. STRONG SPIN-PHOTON COUPLING

The large dipole moment of these quantum dots and their large SOI makes this architecture optimal to strongly couple the hole spin qubit to a superconducting resonators. One viable approach is to couple a long quantum dot to a high-impedance resonator by shaking the dot along the smooth confinement direction. In analogy to Ge/Si core-shell nanowires [18,21], this approach enables a strong spin-photon interaction in a single quantum dot, and it is especially appealing in our system when the magnetic field is applied along the z direction, where the qubit is insensitive to charge noise; see Sec. IV B. In this case, the large direct Rashba SOI linear in momentum p_z [see Eqs. (36) and (37)] enhances the strength of the spin-photon interaction compared to alternative proposals based on cubic SOI [36], potentially resulting in orders of magnitude larger coupling strengths [20]. However, this approach requires a plunger gate misaligned from the center of the quantum dot, reducing the geometric lever arm between the electrode and the dot, and potentially risking the screening of the driving gate by the electrode defining the dot.

In contrast, we now focus here on a different setup that makes use of the alternative driving mechanism discussed in Sec. IV C, where a short quantum dot is shaken in the angular direction. Because this approach relies on a driving field applied in the y direction, perpendicular to the smooth confinement, the plunger electrode can be aligned to the center of the dot, enhancing the lever arm and potentially enabling higher coupling strengths. While we now restrict our analysis to short quantum dots in annular CQWs, we emphasize that the results shown here are also valid for planar CQWs; see Sec. IV D. We remark that our system only requires a *single short quantum dot*, in contrast to different approaches in hole systems where the dipole moment is enlarged by delocalizing the hole over more dots [87].

State-of-the-art high-impedance resonators can be made rather resilient against small magnetic fields, with quality factors $Q \sim 10^5$ at the small magnetic fields $B \lesssim 0.5$ T considered here, and at the same time they reach rather high values of zero-point-fluctuation potential $V_{\rm ZPF} = e\omega_C\sqrt{\hbar Z} \sim 10$–$100$ μeV [23–27]. Here, $Z \sim 1$–10 kΩ is the characteristic impedance of a cavity with resonant frequency $\omega_C/2\pi \approx 5$ GHz.

The Hamiltonian describing this cavity is $H_C = \hbar\omega_C a^\dagger a$, where a and $a^\dagger$ are bosonic ladder operators annihilating and creating a microwave photon in the resonator. At the antinode the quantized electric potential of a single boson is $\hat{V} = V_{\rm ZPF}(a^\dagger + a)$ [88,89]. If the plunger electrode is connected to the antinode of the resonator instead of an external power source then the qubit Hamiltonian in Eq. (24) is still valid, while the ac drive is replaced as $eE_y(t)R \to \alpha V_{\rm ZPF}(a^\dagger + a)$, where α is the lever arm of the electrode. We neglect here the variations of the quantum dot size caused by the gate and assume that the electrode only produces an electric field E_y.

To maximize the qubit-resonator interactions, we consider $\mathbf{B} \parallel y$, resulting in the coupling Hamiltonian $H_{\rm int} = \nu(a^\dagger + a)\sigma_x$ with interaction strength

$$\frac{\nu}{2\pi} = \frac{\omega_B}{2\pi}\frac{\alpha V_{\rm ZPF}}{2\hbar\omega_\varphi}\frac{\delta g_{xy}^y}{g_{yy}}. \tag{40}$$

By considering as in Eq. (33) a strained CQW with radius $R = 20$ nm, $\omega_B/2\pi = 5$ GHz, and $E_x = 0.13$ V/μm, such that $\delta g_{xy}^y/g_{yy} \approx 6$, $g_{yy} = 1.35$, and $B = 0.25$ mT, we find that $\nu \approx 50$ MHz for the realistic values of lever arm $\alpha = 0.4$ and $V_{\rm ZPF} = 20$ μeV [23]. This interaction strength is comparable to that reported in charge qubits [22] and in spin qubits defined in multiple quantum dots [30,31].

Moreover, we note that this system is well within the strong coupling regime. In fact, ν is about 12 times larger than the dephasing rate $1/T_2^* \approx 4.3$ MHz of the qubit (see Sec. IV B and Fig. 6) and 3 orders of magnitude larger than the decay rate of the photon in state-of-the-art cavities, $\omega_C/2\pi Q \approx 50$ kHz.

We emphasize that the values of ν reported here can be further optimized in different ways. Larger values of the ratio $\delta g^y_{xy}/g_{yy}\omega_\varphi$ can be reached by tuning E_x, by increasing the radius R, and, in our device, by also optimizing the electrostatic gate design to maximize the lever arm. Moreover, a stronger coupling strength can be reached at larger cavity and qubit frequencies and higher impedances because $\nu \propto \omega_B\omega_C\sqrt{Z}$. By considering $B = 1$ T [23] and by reducing the length of resonator by 4 times, one obtains more than an order of magnitude larger $\nu/2\pi \approx 800$ MHz at $\omega_B/2\pi \approx 20$ GHz, a frequency still compatible with microwave technology [90,91]. Moreover, resonators with a higher characteristic impedance, approaching the resistance quantum 25 kΩ, could also be conceived, e.g., by using carbon nanotubes [92–94] or quantum Hall edge states [95–98], further enhancing the coupling strength. The latter approach is particularly appealing for our system, because in Ge/SiGe heterostructures well-developed quantum Hall plateaus have recently been observed at magnetic fields below 1 T [99].

For these reasons, in our devices strong spin-photon couplings with interaction strength exceeding a few hundreds of megahertz are realistically achievable with current state-of-the-art technology, offering a way for entangling distant qubits, as well as for high-fidelity single-shot readout schemes.

VII. CONCLUSIONS

In conclusion, in this work we discuss annular and planar curved quantum wells, focusing on their application for spin-based quantum information processing. This architecture takes full advantage of the large SOI of hole nanostructures and the curvature of the cross section enhances the electric dipole moment of the system, and guarantees that the maximal value of the SOI is reached at low values of the externally applied electric field.

We present a detailed model of these devices, discussing several possible implementations and highlighting their key features and their differences from current state-of-the-art hole spin qubits, including their peculiar response to strain and electric field. In a wide range of electric fields, CQWs are to good approximation insensitive to charge noise, a critical issue in current devices, enabling ultrafast high coherent qubit gates at low power, and pushing hole spin qubits towards higher speed and coherence standards.

We also find that in CQWs ultrafast operations can be realized in short quantum dots, with ac driving fields perpendicular to the well. This feature enables a strong interaction between a hole spin confined in a single quantum dot and microwave photons, with interaction strengths that can realistically exceed a few hundreds of megahertz with current technology. CQWs can thus relax the many technological constraints and challenges to reach the strong hole spin-photon coupling regime, and will constitute an effective building block to scale up the next generation of quantum processors.

ACKNOWLEDGMENTS

We thank C. Adelsberger, B. Hetenyi, and H. Legg for useful discussions, and T. Patlatiuk and G. Katsaros for valuable comments and feedback on the manuscript. We are also grateful to G. Gadea Diez and I. Zardo for drawing our attention towards curved quantum wells. This work is supported as a part of NCCR SPIN funded by the Swiss National Science Foundation (Grant No. 51NF40-180604).

APPENDIX A: STRAIN HAMILTONIAN

We present here a more detailed derivation of the strain Hamiltonian in Eq. (4). In general, the effect of strain on the valence band of Si and Ge is modeled by the isotropic BP Hamiltonian [100]

$$H_{\rm BP} = b\sum_i \varepsilon_{ii}J_i^2 + 2b\varepsilon_{xy}\{J_x, J_y\} + \text{c.p.}, \tag{A1}$$

where c.p. stands for cyclic permutations, $b = -2.2$ eV, and ε_{ij} are the elements of the strain tensor.

The strain tensor in the Ge quantum well can be accurately estimated by using classical linear elasticity theory [101], in analogy to Refs. [47,57,102–104]. We consider an infinitely long annular CQW with the cross section sketched in Fig. 1(a). Following Ref. [47], we assume that Si and Ge are isotropic elastic media, where the linear relation between the stress tensor σ_{ij} and the strain tensor ε_{ij} is parametrized by two Lamé parameters λ and μ. The static displacement field $\mathbf{u}$ is related to the strain tensor by $\varepsilon_{ij} = (\partial_i u_j + \partial_j u_i)/2$. In the absence of body forces, the displacement field $\mathbf{u}$ in the material $n = \{\text{Si, Ge}\}$ is static when [101]

$$\mu_n\nabla^2\mathbf{u}^n + (\mu_n + \lambda_n)\nabla(\nabla\cdot\mathbf{u}^n) = 0. \tag{A2}$$

The boundary conditions of this system of equations are extensively discussed in, e.g., Refs. [47,102–104] and they include the absence of forces at the interfaces and the condition of pseudomorphic growth $\mathbf{t}\cdot\mathbf{l}_n = \mathbf{t}\cdot\mathbf{l}_m$, where $\mathbf{t}$ is a tangent vector to the interface and the distorted lattice vectors of the material n, m are

$$\mathbf{l}_{n,m} = a_{n,m}\sum_i \mathbf{e}_i\sum_j(\delta_{ij} + \partial_i u_j^{n,m}), \tag{A3}$$

where $a_{\rm Si} = 0.543$ nm and $a_{\rm Ge} = 0.566$ nm are the lattice constants of Si and Ge, respectively. Finally, a stable

strain configuration minimizes the total elastic energy $U = \frac{1}{2}\sum_n \int d\mathbf{r}(\lambda_n \mathrm{Tr}(\varepsilon^n)^2 + 2\mu_n \sum_{ij}[\varepsilon^n_{ij}]^2)$.

By working in cylindrical coordinates, we find that in the Ge quantum well the strain tensor is diagonal and its diagonal elements read

$$\varepsilon_{rr,\varphi\varphi} = \frac{1}{2}\left(c_1 \pm \frac{R_1^2}{r^2}c_2\right), \qquad \varepsilon_{zz} = \frac{c_3}{2}, \tag{A4}$$

with the c_i being dimensionless constants dependent on the design of the quantum well. Combining this result with Eq. (A1), the BP Hamiltonian reduces to

$$H_{\mathrm{BP}} = J_z^2\epsilon_z - J_r^2\epsilon_r + \left(J_r^2 + \frac{1}{2}J_z^2 - \frac{15}{8}\right)\left(1 - \frac{R^2}{r^2}\right)\epsilon_r. \tag{A5}$$

Neglecting the small corrections arising form the difference in the Lamé parameters of Si and Ge, the energies ϵ_r and ϵ_z can be compactly written as

$$\epsilon_r = \frac{R_1^2}{R^2}|b|c_2 \approx \left(1 - \frac{\tau}{2R}\right)^2 |b|\varepsilon_0, \tag{A6a}$$

$$\epsilon_z = \frac{|b|}{2}\left(c_1 - \frac{R_1^2}{R^2}c_2 - c_3\right) \approx \left(\frac{1}{2} - \frac{\tau}{8R} - \frac{R^2}{R_3^2}\right)\frac{\tau}{R}|b|\varepsilon_0, \tag{A6b}$$

$$\varepsilon_0 = \left(1 + \frac{2\lambda}{\lambda + 2\mu}\right)\varepsilon_{\parallel} \approx 1.6\varepsilon_{\parallel}. \tag{A6c}$$

The expressions obtained by including the differences in the Lamé parameters of Si and Ge are lengthy and we do not report them here. However, we show them with solid lines in Fig. 2, and we find that Eqs. (A6) are rather accurate and nicely reproduce the more general solutions.

Compared to Eqs. (4), Eqs. (A5) present an additional, inhomogeneous radial strain component that is proportional to $1 - R^2/r^2$. This term is completely off-diagonal when the quantization axis is along the z direction and it mixes HH and LH with opposite spins. We note that the matrix elements of the operator $1 - R^2/r^2$ in the basis states in Eq. (11) are $\propto \tau$ and they mix states that are separated by an energy gap of about $\epsilon_c \propto \tau^{-2}$. Consequently, the corrections to the model caused by the inhomogeneous strain scale as $\propto \tau^3$, and because in this work we focus on thin quantum wells, we neglect them in the main text.

APPENDIX B: HAMILTONIAN IN THE ROTATED BASIS

We report here the explicit expressions of the 6×6 LK, magnetic, and BP Hamiltonians including HHs, LHs, and spin-orbit split-off holes (SOHs) [53], after the transformation $U = e^{-i(J_3 \oplus \sigma_3)\varphi} e^{-i(J_2 \oplus \sigma_2)\pi/2}$ that generalizes the rotation discussed in the main text when the SOHs are included. To simplify the notation, for each Hamiltonian H_i, we introduce the decomposition

$$U^\dagger H_i U = \begin{pmatrix} H_i^4 & H_i^{4,2} \\ (H_i^{4,2})^\dagger & H_i^2 \end{pmatrix}. \tag{B1}$$

We also write the equations assuming that the momentum operator always acts first on the wave function, e.g., $r^{-1}k_r \equiv k_r/r \neq k_r r^{-1}$; we also use here the wave-vector operators $k_{\varphi,z} = -i\partial_{\varphi,z}$ and $k_r = -i(\partial_r + 1/2r)$ instead of the momenta $p_i = \hbar k_i$.

Introducing the quantities $\gamma_\pm = \gamma_1 \pm \gamma_s$ and $k_\pm = k_\varphi/r \pm ik_z$ and the SOHs gap Δ_S [53], we find that in the rotated basis the LK Hamiltonian reads

$$H^4_{\mathrm{LK}} = \frac{\hbar^2}{m}\begin{pmatrix} \frac{1}{2}k_r^2(\gamma_1 - 2\gamma_s) + \frac{2\gamma_1-\gamma_s}{8r^2} & 0 & \frac{\sqrt{3}(2\gamma_1-\gamma_s)}{8r^2} + \frac{i\sqrt{3}k_r\gamma_s}{2r} & 0 \\ 0 & \frac{1}{2}k_r^2(\gamma_1 + 2\gamma_s) + \frac{6\gamma_1+9\gamma_s}{8r^2} & 0 & \frac{\sqrt{3}(2\gamma_1+3\gamma_s)}{8r^2} - \frac{i\sqrt{3}k_r\gamma_s}{2r} \\ \frac{\sqrt{3}(2\gamma_1+3\gamma_s)}{8r^2} - \frac{i\sqrt{3}k_r\gamma_s}{2r} & 0 & \frac{1}{2}k_r^2(\gamma_1 + 2\gamma_s) + \frac{6\gamma_1+9\gamma_s}{8r^2} & 0 \\ 0 & \frac{\sqrt{3}(2\gamma_1-\gamma_s)}{8r^2} + \frac{i\sqrt{3}k_r\gamma_s}{2r} & 0 & \frac{1}{2}k_r^2(\gamma_1 - 2\gamma_s) + \frac{2\gamma_1-\gamma_s}{8r^2} \end{pmatrix}$$

$$+ \frac{\hbar^2}{m}\begin{pmatrix} \frac{1}{2}\gamma_+ k_- k_+ & \frac{\sqrt{3}(\gamma_- k_+ + k_-(\gamma_+ + 4irk_r\gamma_s))}{4r} & \frac{1}{2}\sqrt{3}k_-^2\gamma_s & \frac{3k_-\gamma_s}{2r} \\ \frac{\sqrt{3}(\gamma_+ k_- + k_+(\gamma_1 + (3-4irk_r)\gamma_s))}{4r} & \frac{1}{2}\gamma_- k_- k_+ & \frac{\gamma_1(k_- + k_+) + (2k_- - k_+)\gamma_s}{2r} & \frac{1}{2}\sqrt{3}k_-^2\gamma_s \\ \frac{1}{2}\sqrt{3}k_+^2\gamma_s & \frac{\gamma_1(k_- + k_+) - (k_- - 2k_+)\gamma_s}{2r} & \frac{1}{2}\gamma_- k_- k_+ & \frac{\sqrt{3}(\gamma_+ k_+ + k_-(\gamma_1 + (3-4irk_r)\gamma_s))}{4r} \\ \frac{3k_+\gamma_s}{2r} & \frac{1}{2}\sqrt{3}k_+^2\gamma_s & \frac{\sqrt{3}(\gamma_- k_- + k_+(\gamma_+ + 4irk_r\gamma_s))}{4r} & \frac{1}{2}\gamma_+ k_- k_+ \end{pmatrix},$$

$$H^{4,2}_{\mathrm{LK}} = \frac{\hbar^2\gamma_s}{2\sqrt{2}mr}\begin{pmatrix} \sqrt{3}(k_+ - 2ik_- rk_r) & i\sqrt{3}(k_r + 2ik_-^2 r) \\ 2k_- k_+ r - k_r(4rk_r + 3i) & -2k_+ + k_-(-5 + 6irk_r) \\ 2k_- + k_+(5 - 6irk_r) & -2k_- k_+ r + k_r(4rk_r + 3i) \\ \sqrt{3}(2k_+^2 r - ik_r) & -\sqrt{3}(k_- - 2ik_+ rk_r) \end{pmatrix}, \quad H^2_{\mathrm{LK}} = \frac{\hbar^2\gamma_1}{2m}\left[k_+k_- + k_r^2 + \frac{k_\varphi}{r}\sigma_1\right] + \Delta_S.$$

We note that, to explicitly verify that $H_{\rm LK}$ is a Hermitian operator, one needs the relation $[k_r, 1/r] = i/r^2$.

We now report the magnetic Hamiltonian $H_{\mathbf{B}}$ that includes both the Zeeman and orbital magnetic field effects. By using the isotropic LK Hamiltonian and the gauge $\mathbf{A} = (B_y z - B_z y/2, -B_x z + B_z x/2, 0)$, one obtains, to linear order in $\mathbf{B}$,

$$H_{\mathbf{B}} = \mu_B B_z h_z + \mu_B[B_x \cos(\varphi) + B_y \sin(\varphi)]h_+ + \mu_B[B_x \sin(\varphi) - B_y \cos(\varphi)]h_-, \tag{B2}$$

where the dimensionless matrices h_i are given by

$$h_z^4 = \begin{pmatrix} \gamma_+ k_\varphi & \frac{\sqrt{3}}{2}\left[\gamma_1 - 2(\kappa - irk_r\gamma_s - \gamma_s)\right] & \sqrt{3}k_- r\gamma_s & \frac{3\gamma_s}{2} \\ \frac{\sqrt{3}}{2}\left[\gamma_1 - 2(\kappa + irk_r\gamma_s)\right] & \gamma_- k_\varphi & \gamma_1 - 2\kappa + \frac{\gamma_s}{2} & \sqrt{3}k_- r\gamma_s \\ \sqrt{3}k_+ r\gamma_s & \gamma_1 - 2\kappa + \frac{\gamma_s}{2} & \gamma_- k_\varphi & \frac{\sqrt{3}}{2}\left[\gamma_1 - 2(\kappa + irk_r\gamma_s)\right] \\ \frac{3\gamma_s}{2} & \sqrt{3}k_+ r\gamma_s & \frac{\sqrt{3}}{2}\left[\gamma_1 - 2(\kappa - irk_r\gamma_s - \gamma_s)\right] & \gamma_+ k_\varphi \end{pmatrix},$$

$$h_+^4 = \begin{pmatrix} 3\kappa - \frac{2\gamma_+ z k_\varphi}{r} & -\frac{\sqrt{3}z(\gamma_1 + 2irk_r\gamma_s + 2\gamma_s)}{r} & \frac{2i\sqrt{3}\gamma_s\left(r\{z,k_z\} + izk_\varphi\right)}{r} & -\frac{3z\gamma_s}{r} \\ -\frac{\sqrt{3}z(\gamma_1 - 2irk_r\gamma_s)}{r} & \kappa - \frac{2\gamma_- z k_\varphi}{r} & -\frac{z(2\gamma_1 + \gamma_s)}{r} & \frac{2i\sqrt{3}\gamma_s\left(r\{z,k_z\} + izk_\varphi\right)}{r} \\ -\frac{2\sqrt{3}\gamma_s\left(zk_\varphi + ir\{z,k_z\}\right)}{r} & -\frac{z(2\gamma_1 + \gamma_s)}{r} & -\kappa - \frac{2\gamma_- z k_\varphi}{r} & -\frac{\sqrt{3}z(\gamma_1 - 2irk_r\gamma_s)}{r} \\ -\frac{3z\gamma_s}{r} & -\frac{2\sqrt{3}\gamma_s\left(zk_\varphi + ir\{z,k_z\}\right)}{r} & -\frac{\sqrt{3}z(\gamma_1 + 2irk_r\gamma_s + 2\gamma_s)}{r} & -3\kappa - \frac{2\gamma_+ z k_\varphi}{r} \end{pmatrix},$$

$$h_-^4 = \begin{pmatrix} -\frac{z[\gamma_1(2rk_r + i) + (-4rk_r + i)\gamma_s]}{r} & \frac{\sqrt{3}\left(-2izk_\varphi\gamma_s + i\kappa r - 2r\{z,k_z\}\gamma_s\right)}{r} & -\frac{2i\sqrt{3}z\gamma_s}{r} & 0 \\ \frac{i\sqrt{3}\left(2zk_\varphi\gamma_s - \kappa r + 2ir\{z,k_z\}\gamma_s\right)}{r} & -\frac{z[\gamma_1(2rk_r + i) + (4rk_r - i)\gamma_s]}{r} & 2i\kappa & 0 \\ 0 & -2i\kappa & -\frac{z[\gamma_1(2rk_r + i) + (4rk_r - i)\gamma_s]}{r} & \frac{\sqrt{3}\left(2izk_\varphi\gamma_s + i\kappa r + 2r\{z,k_z\}\gamma_s\right)}{r} \\ 0 & -\frac{2i\sqrt{3}z\gamma_s}{r} & \frac{\sqrt{3}\left(-2izk_\varphi\gamma_s - i\kappa r + 2r\{z,k_z\}\gamma_s\right)}{r} & -\frac{z[\gamma_1(2rk_r + i) + (-4rk_r + i)\gamma_s]}{r} \end{pmatrix},$$

$$h_z^{4,2} = \begin{pmatrix} \frac{1}{2}\sqrt{\frac{3}{2}}\left(2\kappa - \gamma_s - 2irk_r\gamma_s\right) & -\sqrt{6}k_- r\gamma_s \\ \sqrt{2}rk_\varphi\gamma_s & \frac{2\kappa - \gamma_s + 6irk_r\gamma_s}{2\sqrt{2}} \\ \frac{-2\kappa - 6irk_r\gamma_s + \gamma_s}{2\sqrt{2}} & -\sqrt{2}rk_\varphi\gamma_s \\ \sqrt{6}k_+ r\gamma_s & \frac{1}{2}\sqrt{\frac{3}{2}}\left(-2\kappa + 2irk_r\gamma_s + \gamma_s\right) \end{pmatrix}, \quad h_z^2 = \gamma_1 k_\varphi - \sigma_1(2\kappa - \gamma_1/2)\,,$$

$$h_+^{4,2} = \frac{1}{r}\begin{pmatrix} \sqrt{\frac{3}{2}}z\left(1 + 2irk_r\right)\gamma_s & 2\sqrt{6}\gamma_s\left(zk_\varphi - ir\{z,k_z\}\right) \\ \sqrt{2}\left(\kappa r - 2zk_\varphi\gamma_s\right) & \frac{z(1 - 6irk_r)\gamma_s}{\sqrt{2}} \\ \frac{z(-1 + 6irk_r)\gamma_s}{\sqrt{2}} & \sqrt{2}\left(2zk_\varphi\gamma_s + \kappa r\right) \\ -2\sqrt{6}\gamma_s\left(zk_\varphi + ir\{z,k_z\}\right) & \sqrt{\frac{3}{2}}z\left(-1 - 2irk_r\right)\gamma_s \end{pmatrix}, \quad h_+^2 = -\begin{pmatrix} -2\kappa + \frac{2\gamma_1 z k_\varphi}{r} & \frac{\gamma_1 z}{r} \\ \frac{\gamma_1 z}{r} & 2\kappa + \frac{2\gamma_1 z k_\varphi}{r} \end{pmatrix},$$

$$h_-^{4,2} = \frac{\sqrt{3}}{\sqrt{2}r}\begin{pmatrix} 2izk_\varphi\gamma_s - i\kappa r + 2r\{z,k_z\}\gamma_s & iz\gamma_s \\ \frac{z(8rk_r + i)\gamma_s}{\sqrt{3}} & -\frac{6izk_\varphi\gamma_s + i\kappa r + 6r\{z,k_z\}\gamma_s}{\sqrt{3}} \\ \frac{i\left(6zk_\varphi\gamma_s - \kappa r + 6ir\{z,k_z\}\gamma_s\right)}{\sqrt{3}} & -\frac{z(8rk_r + i)\gamma_s}{\sqrt{3}} \\ -iz\gamma_s & -2izk_\varphi\gamma_s - i\kappa r + 2r\{z,k_z\}\gamma_s \end{pmatrix},$$

$$h_-^2 = -\begin{pmatrix} \frac{\gamma_1 z(2rk_r + i)}{r} & -2i\kappa \\ 2i\kappa & \frac{\gamma_1 z(2rk_r + i)}{r} \end{pmatrix}.$$

To explicitly verify the Hermiticity of $H_{\mathbf{B}}$, one needs $[k_\varphi, \cos(\varphi)] = i\sin(\varphi)$ and $[k_\varphi, \sin(\varphi)] = -i\cos(\varphi)$.

Finally, neglecting the inhomogeneous component of strain, the 6×6 rotated BP Hamiltonian is

$$H_{\rm BP} = \begin{pmatrix} \frac{3}{4}(\epsilon_z - 3\epsilon_r) & 0 & \frac{\sqrt{3}\epsilon_z}{2} & 0 & 0 & -\sqrt{\frac{3}{2}}\epsilon_z \\ 0 & \frac{1}{4}(7\epsilon_z - \epsilon_r) & 0 & \frac{\sqrt{3}\epsilon_z}{2} & -\frac{2\epsilon_r+\epsilon_z}{\sqrt{2}} & 0 \\ \frac{\sqrt{3}\epsilon_z}{2} & 0 & \frac{1}{4}(7\epsilon_z - \epsilon_r) & 0 & 0 & \frac{2\epsilon_r+\epsilon_z}{\sqrt{2}} \\ 0 & \frac{\sqrt{3}\epsilon_z}{2} & 0 & \frac{3}{4}(\epsilon_z - 3\epsilon_r) & \sqrt{\frac{3}{2}}\epsilon_z & 0 \\ 0 & -\frac{2\epsilon_r+\epsilon_z}{\sqrt{2}} & 0 & \sqrt{\frac{3}{2}}\epsilon_z & \frac{5}{4}(\epsilon_z - \epsilon_r) & 0 \\ -\sqrt{\frac{3}{2}}\epsilon_z & 0 & \frac{2\epsilon_r+\epsilon_z}{\sqrt{2}} & 0 & 0 & \frac{5}{4}(\epsilon_z - \epsilon_r) \end{pmatrix}. \tag{B3}$$

APPENDIX C: SPLIT-OFF HOLES

The valence band of cubic semiconductors comprises the HH and LH bands, degenerate at the Γ point, and a third band that is split-off by bulk SOI. In Ge these SOHs are separated from the HHs and LHs by $\Delta_S \approx 300$ meV [53]. Our treatment can be generalized to include this additional band by the 6×6 LK Hamiltonian reported in Appendix B. The effective theory described by Eqs. (12) and (23) is still qualitatively valid, but the parameters in Eqs. (13) are quantitatively modified by Δ_S. We find that the SOHs enhance the coupling of the hole spin to photons in microwave resonators.

Because of Δ_S, in the presence of a large longitudinal strain ϵ_z a second-order perturbation theory does not suffice to accurately reproduce the spectrum. A good estimate of the effective parameters requires terms up to fourth order in Schrieffer-Wolff perturbation theory. The complete expressions of the parameters are lengthy and we do not report them here; however, by only keeping the most relevant terms, one can simplify the expressions as

$$\frac{m}{m^*} \approx \gamma_1 + \gamma_s - 3\tilde{\gamma}_S, \tag{C1a}$$

$$\frac{m}{\delta m} \approx 3\gamma_s \left[\left(1 + 5\frac{\gamma_s\epsilon_c + \gamma_1\epsilon_r}{\gamma_1\epsilon_z}\tilde{\epsilon}_z^{\Delta} \right)\tilde{\epsilon}_z \right. \tag{C1b}$$

$$\left. + 2\left(1 + \frac{\gamma_s\epsilon_c + \gamma_1\epsilon_r}{\gamma_1\epsilon_z}\tilde{\epsilon}_z^{\Delta} \right)\tilde{\epsilon}_z^{\Delta} \right], \tag{C1c}$$

$$v_- \approx \frac{3\hbar}{2mR}\left[\gamma_s - \tilde{\gamma}_S - \left(\frac{\gamma_1}{2} + \gamma_s \right)\tilde{\epsilon}_z - \frac{3}{4}\left(\gamma_1 + \gamma_s \right)\tilde{\epsilon}_z^{\Delta} \right], \tag{C1d}$$

$$v_+ \approx \frac{3\hbar}{4mR}\left[\gamma_1\tilde{\epsilon}_z + \frac{3}{2}\left(\gamma_1 + \gamma_s \right)\tilde{\epsilon}_z^{\Delta} \right], \tag{C1e}$$

where we introduced the renormalized quantities

$$\tilde{\gamma}_S = \tilde{\gamma} + \tilde{\gamma}_\Delta + \frac{9\pi^2}{8\gamma_s}\tilde{\gamma}\tilde{\gamma}_\Delta\left[\frac{9\pi^2}{32\gamma_s}(\tilde{\gamma} + \tilde{\gamma}_\Delta) - 1 \right], \tag{C2a}$$

$$\tilde{\gamma}_\Delta = \frac{128}{9\pi^2}\frac{\gamma_s}{2 + \gamma_1(3\epsilon_c + 2\Delta_S + 2\epsilon_r + \epsilon_z)/\gamma_s\epsilon_c}, \tag{C2b}$$

$$\tilde{\epsilon}_z^{\Delta} = \frac{2\epsilon_z}{\epsilon_z + 2(\Delta_S + \epsilon_r) + 2\gamma_s\epsilon_c/\gamma_1}. \tag{C2c}$$

The Zeeman interactions in Eq. (23) are also quantitatively modified by Δ_S and they read

$$\begin{aligned} \frac{H_B}{3\kappa\mu_B} &= B_z\left[\left(\tilde{\epsilon}_z^S + \frac{1}{2}\frac{\tilde{\kappa}_S}{\kappa} \right)\sigma_x + \frac{1}{3\kappa}\frac{m}{m_\varphi}p_\varphi \right] \\ &+ [B_x\cos(\varphi) + B_y\sin(\varphi)] \\ &\times \left[\left(1 - \frac{\tilde{\gamma}_S}{\kappa} \right)\sigma_z - \frac{\tilde{\kappa}_S}{\kappa}\frac{z}{R}\sigma_x \right] \\ &+ [B_x\sin(\varphi) - B_y\cos(\varphi)]\tilde{\epsilon}_z^S\sigma_y, \end{aligned} \tag{C3}$$

where, in analogy to Eq. (17), we define $\tilde{\kappa}_S = 2mRv_\varphi/3\hbar$. Here, $v_\varphi = v_- - v_+$ and $m_\varphi = (1/m_* - 1/\delta m)^{-1}$ both include the corrections caused by Δ_S. The longitudinal strain modifies the Zeeman energy via the dimensionless parameter

$$\begin{aligned} \tilde{\epsilon}_z^S &= \tilde{\epsilon}_z - \tilde{\epsilon}_z^{\Delta} \\ &+ \frac{\gamma_s\epsilon_c + \gamma_1\epsilon_r}{\gamma_1\epsilon_z}\tilde{\epsilon}_z^{\Delta}\tilde{\epsilon}_z\left[1 + 2\frac{\gamma_s\epsilon_c + \gamma_1\epsilon_r}{\gamma_1\epsilon_z}(\tilde{\epsilon}_z - \tilde{\epsilon}_z^{\Delta}) \right]. \end{aligned} \tag{C4}$$

As expected, in the limit $\Delta_S \to \infty$, we recover the equations reported in the main text.

We also remark that the equations of g-factors and Rabi frequencies in Secs. IV and V are straightforwardly modified in the presence of a significant contribution of the SOHs by substituting $\tilde{\kappa} \to \tilde{\kappa}_S$, $\tilde{\epsilon}_z \to \tilde{\epsilon}_z^S$, and $\tilde{\gamma} \to \tilde{\gamma}_S$, and by using the SOI velocities and masses defined in Eqs. (C1). Moreover, we stress that Eqs. (C1) and (C3) are not only valid for Ge, but they are also applicable to other semiconductors, such as GaAs, InAs, and InSb, by using the appropriate material-dependent parameters [53].

In Fig. 11 we show the effect of the SOHs on the effective parameters, also including a comparison between

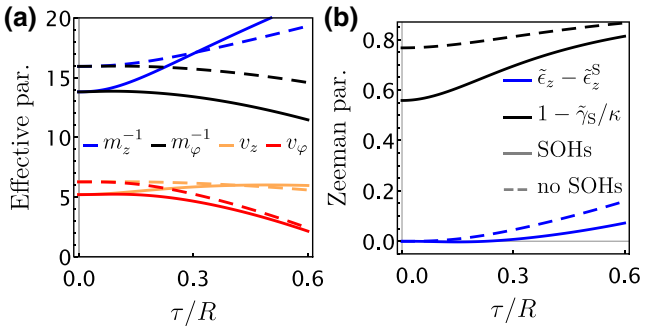

FIG. 11. Effect of the SOHs on the parameters of the effective theory in Eq. (12) of a thin Ge CQW. With dashed lines we show results obtained by neglecting the SOHs; see Eqs. (13). Solid lines and thin dotted lines represent results obtained by including corrections coming from Δ_S. In particular, thin dashed lines show the expressions in Eqs. (C1), while solid lines show the complete results for the parameters to fourth order in the Schrieffer-Wolff transformation. We consider here a thin quantum well with radius $R = 20$ nm and vary the strain as a function of τ according to Eqs. (5). For simplicity, we consider here a thick outer shell with $R_3 \gg R$. The mass $m_{z,\varphi} = (1/m^* \pm 1/\delta m)^{-1}$ and the SOI $v_{z,\varphi} = v_- \pm v_+$ are shown in units of m and $\hbar/mR$, respectively.

the simple expressions reported in Eqs. (C1) and the full expressions. We show the relevant quantities $m_{z,\varphi} = (1/m_* \pm 1/\delta m)^{-1}$, $v_{z,\varphi} = v_- \pm v_+$ and the Zeeman parameters $\tilde{\epsilon}_z^S$ and $1 - \tilde{\gamma}_S/\kappa$. We note that the Zeeman parameters and v_z are not significantly affected by the SOHs, but the masses $m_{z,\varphi}$ and v_φ are strongly renormalized by Δ_S, especially in the presence of a large longitudinal strain ϵ_z.

At low electric fields, the lower values of v_φ due to the SOHs result in a smaller SOI-induced gap $\Delta = \hbar v_\varphi/R$; see Eq. (17). However, as argued in the text, this gap becomes dominated by external electric field E_x and already at weak values of E_x it approaches $\omega_E \propto 1/\sqrt{m_\varphi}$; see Eq. (21). This energy gap becomes smaller because the value of m_φ is increased by the SOHs; however, the gap remains in the millielectron volt range for the parameters examined. For example, at $R = 20$ nm, $\tau = 10$ nm, and large strain ($R_3 \to \infty$), ω_E is reduced by the multiplicative factor $\sqrt{m_\varphi(\Delta_S \to \infty)/m_\varphi} \approx 0.8$; see Fig. 11.

We find that the SOHs can be beneficial to reach even higher values of spin-resonator coupling. In fact, in the low electric field limit, the susceptibility of the spin qubit to the electric field is enhanced by the SOHs, because $\delta g^{x,y} \propto \sin(\theta_E)$ [see Eqs. (32) and (34)], and the angle $\theta_E = \arctan[eE_xR/\Delta\cos(\theta_z)]$ becomes larger by the reduced values of Δ; the prefactor of these equations is also enhanced by the larger mass m_φ. While these additional contributions are found to improve the performance of the qubit, to simplify the discussion, in the main text we do not examine them.

APPENDIX D: ANISOTROPIC CORRECTIONS

We analyze here some additional properties of the system that go beyond the isotropic LK Hamiltonian in Eq. (2). In particular, we numerically study the role of the anisotropies of the cubic lattice and variations from a circular cross section. Because of these anisotropies, there are some energetically favored directions where the hole is more likely to localize, and thus the electric field response becomes oscillatory depending on the direction of **E**. By investigating separately cubic and cross-section anisotropies, we verify that these oscillations have a rather small amplitude and that our theory based on the isotropic LK Hamiltonian and circular cross sections remains reasonably accurate in more general cases.

The cubic anisotropies of the LK Hamiltonian are small in Ge because $(\gamma_3 - \gamma_2)/\gamma_1 \approx 0.1$; however, because they break the rotation symmetry of Eq. (2), they induce qualitatively different terms in the effective Hamiltonian in Eq. (12). Because of these terms, the total angular momentum is not conserved even without external fields. The amplitude and form of these terms depend on the growth direction of the well. Here, we restrict ourselves to the analysis of CQWs grown along the a main crystallographic axis, e.g., $z \parallel [001]$, and we show that the additional terms $\propto \gamma_3 - \gamma_2$ only result in an additional small correction to the effective theory presented in Sec. IV.

In Fig. 12(a), we show the effect of the cubic anisotropies of the LK Hamiltonian on the g-factor of a short quantum dot with $l_z = R$. We restrict our analysis here to the g-factor obtained for magnetic fields that are perpendicular to the quantum well; a detailed analysis of g_{zz} for different growth directions is provided in Ref. [65]. Qualitatively, we observe a similar behavior to that described in the main text. At $E = 0$ the g-factor in the $x \parallel [100]$ and $y \parallel [010]$ directions coincide, and at larger values of E, the g-factor is increased (decreased) when $\mathbf{B} \parallel \mathbf{E}$ ($\mathbf{B} \perp \mathbf{E}$). However, by rotating the electric field from the main crystallographic axes by an angle φ_e, we observe that the LK anisotropies result in an additional oscillation with period $\pi/2$ superimposed to the isotropic response; see Fig. 5. We note that these oscillations have a larger amplitude and a less sinusoidal shape at larger values of E. We also find similar oscillations on top of the isotropic response in the driving terms $\delta g_{ij}^{x,y}$.

Similar oscillations are found if the cross section is not circular. For example, in Fig. 12(b), we show the g-factor of a short quantum dot defined in a thin Ge quantum well with a square cross section. To investigate the role of cross-section anisotropy, we show here results obtained by using the isotropic LK Hamiltonian. We note that the g-factor in this case is qualitatively similar to the g-factor in Fig. 12(a), with only some small quantitative differences coming from the different cross sections. In particular, because of the fourfold rotational symmetry of the square,

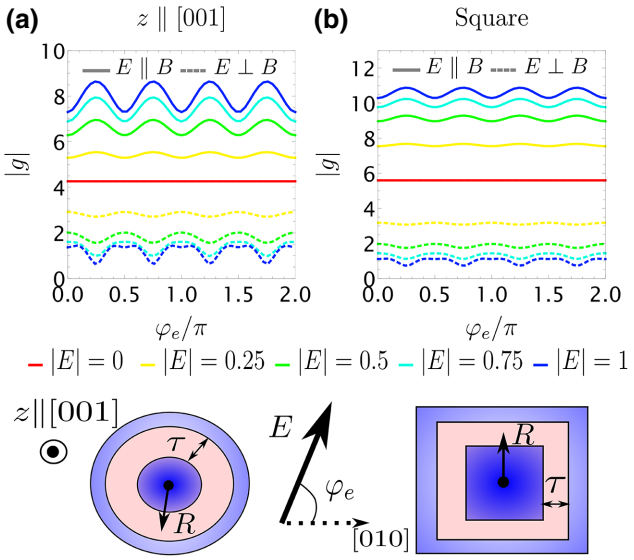

FIG. 12. Effect of the anisotropies on the g-factors of a hole spin qubit in a Ge CQW. We show with solid and dashed lines the total $|g|$-factor obtained when **B** is parallel and perpendicular to E, respectively. We observe oscillations of $|g|$ as a function of the angle φ_e. These oscillations are comparable in panels (a) and (b), where we show a cylindrical quantum well grown along the $z \parallel [001]$ direction and a quantum well with square cross section, respectively. The setup considered is shown at the bottom of the plots. In both cases, we consider $\epsilon_r = 3\epsilon_z = \epsilon_c$, $\tau = R/2$, and $l_z = R$. The values of the electric field are given in units of $\hbar\omega_\varphi/eR$.

the g-factor in this qubit is also oscillating as a function of φ_e with period $\pi/2$ and the oscillations caused by the square cross section have a small amplitude that increases at larger E. Because these oscillations are rather small corrections to isotropic theory, we believe that our theory accurately describes a wide range of devices.

[1] G. Scappucci, C. Kloeffel, F. A. Zwanenburg, D. Loss, M. Myronov, J.-J. Zhang, S. De Franceschi, G. Katsaros, and M. Veldhorst, The germanium quantum information route, Nat. Rev. Mater. **6**, 926 (2021).

[2] M. F. Gonzalez-Zalba, S. de Franceschi, E. Charbon, T. Meunier, M. Vinet, and A. S. Dzurak, Scaling silicon-based quantum computing using CMOS technology, Nat. Electron. **4**, 872 (2021).

[3] N. Hendrickx, D. Franke, A. Sammak, G. Scappucci, and M. Veldhorst, Fast two-qubit logic with holes in germanium, Nature **577**, 487 (2020).

[4] N. W. Hendrickx, W. I. L. Lawrie, M. Russ, F. van Riggelen, S. L. de Snoo, R. N. Schouten, A. Sammak, G. Scappucci, and M. Veldhorst, A four-qubit germanium quantum processor, Nature **591**, 580 (2021).

[5] D. Jirovec, A. Hofmann, A. Ballabio, P. M. Mutter, G. Tavani, M. Botifoll, A. Crippa, J. Kukucka, O. Sagi, F. Martins, J. Saez-Mollejo, I. Prieto, M. Borovkov, J. Arbiol, D. Chrastina, G. Isella, and G. Katsaros, A singlet-triplet hole spin qubit in planar Ge, Nat. Mater. **20**, 1106 (2021).

[6] R. Maurand, X. Jehl, D. Kotekar-Patil, A. Corna, H. Bohuslavskyi, R. Laviéville, L. Hutin, S. Barraud, M. Vinet, M. Sanquer, and S. De Franceschi, A CMOS silicon spin qubit, Nat. Commun. **7**, 1 (2016).

[7] L. C. Camenzind, S. Geyer, A. Fuhrer, R. J. Warburton, D. M. Zumbühl, and A. V. Kuhlmann, A hole spin qubit in a fin field-effect transistor above 4 kelvin, Nat. Electron. **5**, 178 (2022).

[8] N. Piot, B. Brun, V. Schmitt, S. Zihlmann, V. P. Michal, A. Apra, J. C. Abadillo-Uriel, X. Jehl, B. Bertrand, H. Niebojewski, L. Hutin, M. Vinet, M. Urdampilleta, T. Meunier, Y.-M. Niquet, R. Maurand, and S. D. Franceschi, A single hole spin with enhanced coherence in natural silicon, Nat. Nanotechnol. (2022).

[9] J. Fischer, W. A. Coish, D. V. Bulaev, and D. Loss, Spin decoherence of a heavy hole coupled to nuclear spins in a quantum dot, Phys. Rev. B **78**, 155329 (2008).

[10] J. H. Prechtel, A. V. Kuhlmann, J. Houel, A. Ludwig, S. R. Valentin, A. D. Wieck, and R. J. Warburton, Decoupling a hole spin qubit from the nuclear spins, Nat. Mater. **15**, 981 (2016).

[11] R. J. Warburton, Single spins in self-assembled quantum dots, Nat. Mater. **12**, 483 (2013).

[12] S. Bosco and D. Loss, Fully Tunable Hyperfine Interactions of Hole Spin Qubits in Si and Ge Quantum Dots, Phys. Rev. Lett. **127**, 190501 (2021).

[13] D. V. Bulaev and D. Loss, Electric Dipole Spin Resonance for Heavy Holes in Quantum Dots, Phys. Rev. Lett. **98**, 097202 (2007).

[14] F. N. M. Froning, L. C. Camenzind, O. A. H. van der Molen, A. Li, E. P. A. M. Bakkers, D. M. Zumbühl, and F. R. Braakman, Ultrafast hole spin qubit with gate-tunable spin–orbit switch functionality, Nat. Nanotechnol. **16**, 308 (2021).

[15] K. Wang, G. Xu, F. Gao, H. Liu, R.-L. Ma, X. Zhang, Z. Wang, G. Cao, T. Wang, J.-J. Zhang, D. Culcer, X. Hu, H.-W. Jiang, H.-O. Li, G.-C. Guo, and G.-P. Guo, Ultrafast coherent control of a hole spin qubit in a germanium quantum dot, Nat. Commun. **13**, 206 (2022).

[16] H. Watzinger, J. Kukučka, L. Vukušić, F. Gao, T. Wang, F. Schäffler, J.-J. Zhang, and G. Katsaros, A germanium hole spin qubit, Nat. Commun. **9**, 3902 (2018).

[17] C. Kloeffel, M. Trif, and D. Loss, Strong spin-orbit interaction and helical hole states in Ge/Si nanowires, Phys. Rev. B **84**, 195314 (2011).

[18] C. Kloeffel, M. Trif, P. Stano, and D. Loss, Circuit QED with hole-spin qubits in Ge/Si nanowire quantum dots, Phys. Rev. B **88**, 241405 (2013).

[19] C. Kloeffel, M. J. Rančić, and D. Loss, Direct Rashba spin-orbit interaction in Si and Ge nanowires with different growth directions, Phys. Rev. B **97**, 235422 (2018).

[20] S. Bosco, M. Benito, C. Adelsberger, and D. Loss, Squeezed hole spin qubits in Ge quantum dots with ultrafast gates at low power, Phys. Rev. B **104**, 115425 (2021).

[21] S. Bosco, P. Scarlino, J. Klinovaja, and D. Loss, Fully Tunable Longitudinal Spin-Photon Interactions in Si and Ge Quantum Dots, Phys. Rev. Lett. **129**, 066801 (2022).

[22] A. Stockklauser, P. Scarlino, J. V. Koski, S. Gasparinetti, C. K. Andersen, C. Reichl, W. Wegscheider, T. Ihn, K. Ensslin, and A. Wallraff, Strong Coupling Cavity QED with Gate-Defined Double Quantum Dots Enabled by a High Impedance Resonator, Phys. Rev. X **7**, 011030 (2017).

[23] N. Samkharadze, A. Bruno, P. Scarlino, G. Zheng, D. P. DiVincenzo, L. DiCarlo, and L. M. K. Vandersypen, High-Kinetic-Inductance Superconducting Nanowire Resonators for Circuit QED in a Magnetic Field, Phys. Rev. Appl. **5**, 044004 (2016).

[24] L. Grünhaupt, M. Spiecker, D. Gusenkova, N. Maleeva, S. T. Skacel, I. Takmakov, F. Valenti, P. Winkel, H. Rotzinger, W. Wernsdorfer, A. V. Ustinov, and I. M. Pop, Granular aluminium as a superconducting material for high-impedance quantum circuits, Nat. Mater. **18**, 816 (2019).

[25] N. Maleeva, L. Grünhaupt, T. Klein, F. Levy-Bertrand, O. Dupre, M. Calvo, F. Valenti, P. Winkel, F. Friedrich, W. Wernsdorfer, A. V. Ustinov, H. Rotzinger, A. Monfardini, M. V. Fistul, and I. M. Pop, Circuit quantum electrodynamics of granular aluminum resonators, Nat. Commun. **9**, 3889 (2018).

[26] D. Niepce, J. Burnett, and J. Bylander, High Kinetic Inductance NbN Nanowire Superinductors, Phys. Rev. Appl. **11**, 044014 (2019).

[27] L. Grünhaupt, N. Maleeva, S. T. Skacel, M. Calvo, F. Levy-Bertrand, A. V. Ustinov, H. Rotzinger, A. Monfardini, G. Catelani, and I. M. Pop, Loss Mechanisms and Quasiparticle Dynamics in Superconducting Microwave Resonators Made of Thin-Film Granular Aluminum, Phys. Rev. Lett. **121**, 117001 (2018).

[28] L. M. K. Vandersypen, H. Bluhm, J. S. Clarke, A. S. Dzurak, R. Ishihara, A. Morello, D. J. Reilly, L. R. Schreiber, and M. Veldhorst, Interfacing spin qubits in quantum dots and donors—hot, dense, and coherent, Npj Quantum Inf. **3**, 1 (2017).

[29] S. E. Nigg, A. Fuhrer, and D. Loss, Superconducting Grid-Bus Surface Code Architecture for Hole-Spin Qubits, Phys. Rev. Lett. **118**, 147701 (2017).

[30] A. J. Landig, J. V. Koski, P. Scarlino, U. C. Mendes, A. Blais, C. Reichl, W. Wegscheider, A. Wallraff, K. Ensslin, and T. Ihn, Coherent spin–photon coupling using a resonant exchange qubit, Nature **560**, 179 (2018).

[31] X. Mi, M. Benito, S. Putz, D. M. Zajac, J. M. Taylor, G. Burkard, and J. R. Petta, A coherent spin–photon interface in silicon, Nature **555**, 599 (2018).

[32] J. J. Viennot, M. C. Dartiailh, A. Cottet, and T. Kontos, Coherent coupling of a single spin to microwave cavity photons, Science **349**, 408 (2015).

[33] P. Harvey-Collard, J. Dijkema, G. Zheng, A. Sammak, G. Scappucci, and L. M. K. Vandersypen, Coherent Spin-Spin Coupling Mediated by Virtual Microwave Photons, Phys. Rev. X **12**, 021026 (2022).

[34] M. Benito, X. Croot, C. Adelsberger, S. Putz, X. Mi, J. R. Petta, and G. Burkard, Electric-field control and noise protection of the flopping-mode spin qubit, Phys. Rev. B **100**, 125430 (2019).

[35] C. G. L. Bøttcher, S. P. Harvey, S. Fallahi, G. C. Gardner, M. J. Manfra, U. Vool, S. D. Bartlett, and A. Yacoby, Parametric longitudinal coupling between a high-impedance superconducting resonator and a semiconductor quantum dot singlet-triplet spin qubit, Nat. Commun. **13**, 4773 (2022).

[36] P. M. Mutter and G. Burkard, Cavity control over heavy-hole spin qubits in inversion-symmetric crystals, Phys. Rev. B **102**, 205412 (2020).

[37] V. Michal, J. Abadillo-Uriel, S. Zihlmann, R. Maurand, Y.-M. Niquet, and M. Filippone, Tunable hole spin-photon interaction based on g-matrix modulation, arXiv:2204.00404 (2022).

[38] L. J. Lauhon, M. S. Gudiksen, D. Wang, and C. M. Lieber, Epitaxial core–shell and core–multishell nanowire heterostructures, Nature **420**, 57 (2002).

[39] S. Bosco, B. Hetényi, and D. Loss, Hole Spin Qubits in Si FinFETs with Fully Tunable Spin-Orbit Coupling and Sweet Spots for Charge Noise, PRX Quantum **2**, 010348 (2021).

[40] Z. Wang, E. Marcellina, A. R. Hamilton, J. H. Cullen, S. Rogge, J. Salfi, and D. Culcer, Optimal operation points for ultrafast, highly coherent Ge hole spin-orbit qubits, Npj Quantum Inf. **7**, 54 (2021).

[41] O. Malkoc, P. Stano, and D. Loss, Charge-noise induced dephasing in silicon hole-spin qubits, arXiv:2201.06181 (2022).

[42] H. F. Legg, D. Loss, and J. Klinovaja, Majorana bound states in topological insulators without a vortex, Phys. Rev. B **104**, 165405 (2021).

[43] H. F. Legg, M. Rößler, F. Münning, D. Fan, O. Breunig, A. Bliesener, G. Lippertz, A. Uday, A. A. Taskin, D. Loss, J. Klinovaja, and Y. Ando, Giant magnetochiral anisotropy from quantum-confined surface states of topological insulator nanowires, Nat. Nanotechnol. **17**, 696 (2022).

[44] K. Laubscher and J. Klinovaja, Majorana bound states in semiconducting nanostructures, J. Appl. Phys. **130**, 081101 (2021).

[45] F. Maier, J. Klinovaja, and D. Loss, Majorana fermions in Ge/Si hole nanowires, Phys. Rev. B **90**, 195421 (2014).

[46] Stephan G. J. Philips, Mateusz T. Mądzik, Sergey V. Amitonov, Sander L. de Snoo, M. Russ, N. Kalhor, C. Volk, William I. L. Lawrie, D. Brousse, L. Tryputen, B. P. Wuetz, A. Sammak, M. Veldhorst, G. Scappucci, and Lieven M. K. Vandersypen, Universal control of a six-qubit quantum processor in silicon, Nature **609**, 919 (2022).

[47] C. Kloeffel, M. Trif, and D. Loss, Acoustic phonons and strain in core/shell nanowires, Phys. Rev. B **90**, 115419 (2014).

[48] Y.-M. Niquet, C. Delerue, and C. Krzeminski, Effects of strain on the carrier mobility in silicon nanowires, Nano Lett. **12**, 3545 (2012).

[49] K. Moratis, J. Cibert, D. Ferrand, and Y.-M. Niquet, Light hole states in a strained quantum dot: Numerical calculation and phenomenological models, Phys. Rev. B **103**, 245304 (2021).

[50] C. Jia, Z. Lin, Y. Huang, and X. Duan, Nanowire electronics: From nanoscale to macroscale, Chem. Rev. **119**, 9074 (2019).

[51] M. Veldhorst, H. G. J. Eenink, C. H. Yang, and A. S. Dzurak, Silicon CMOS architecture for a spin-based quantum computer, Nat. Commun. **8**, 1766 (2017).

[52] F. N. M. Froning, M. J. Rančić, B. Hetényi, S. Bosco, M. K. Rehmann, A. Li, E. P. A. M. Bakkers, F. A. Zwanenburg, D. Loss, D. M. Zumbühl, and F. R. Braakman, Strong spin-orbit interaction and g-factor renormalization of hole spins in Ge/Si nanowire quantum dots, Phys. Rev. Res. **3**, 013081 (2021).

[53] R. Winkler, *Spin–Orbit Coupling Effects in Two-Dimensional Electron and Hole Systems*, edited by G. Höhler, J. H. Kühn, T. Müller, J. Trümper, A. Ruckenstein, P. Wölfle, and F. Steiner, Springer Tracts in Modern Physics, Vol. 191 (Springer Berlin Heidelberg, Berlin, Heidelberg, 2003).

[54] F. Gao, J.-H. Wang, H. Watzinger, H. Hu, M. J. Rančić, J.-Y. Zhang, T. Wang, Y. Yao, G.-L. Wang, J. Kukučka, L. Vukušić, C. Kloeffel, D. Loss, F. Liu, G. Katsaros, and J.-J. Zhang, Site-controlled uniform Ge/Si hut wires with electrically tunable spin–orbit coupling, Adv. Mater. **32**, 1906523 (2020).

[55] L. A. Terrazos, E. Marcellina, Z. Wang, S. N. Coppersmith, M. Friesen, A. R. Hamilton, X. Hu, B. Koiller, A. L. Saraiva, D. Culcer, and R. B. Capaz, Theory of hole-spin qubits in strained germanium quantum dots, Phys. Rev. B **103**, 125201 (2021).

[56] H. Watzinger, C. Kloeffel, L. Vukusic, M. D. Rossell, V. Sessi, J. Kukucka, R. Kirchschlager, E. Lausecker, A. Truhlar, M. Glaser, A. Rastelli, A. Fuhrer, D. Loss, and G. Katsaros, Heavy-hole states in germanium hut wires, Nano Lett. **16**, 6879 (2016).

[57] B. K. Ridley, W. J. Schaff, and L. F. Eastman, Theoretical model for polarization superlattices: Energy levels and intersubband transitions, J. Appl. Phys. **94**, 3972 (2003).

[58] The strain of a Ge/Si core-shell nanowire with inner radius R_1 and outer radius R_2 is straightforwardly related to the strain in the thin Ge CQW [Eqs. (5)] by the substitutions $\tau/R \to 2$ and $R/R_3 \to R_1/2R_2$.

[59] S. Bravyi, D. P. DiVincenzo, and D. Loss, Schrieffer–Wolff transformation for quantum many-body systems, Ann. Phys. (N. Y) **326**, 2793 (2011).

[60] N. Ares, G. Katsaros, V. N. Golovach, J. J. Zhang, A. Prager, L. I. Glazman, O. G. Schmidt, and S. De Franceschi, SiGe quantum dots for fast hole spin Rabi oscillations, Appl. Phys. Lett. **103**, 263113 (2013).

[61] A. Crippa, R. Maurand, L. Bourdet, D. Kotekar-Patil, A. Amisse, X. Jehl, M. Sanquer, R. Laviéville, H. Bohuslavskyi, L. Hutin, S. Barraud, M. Vinet, Y.-M. Niquet, and S. De Franceschi, Electrical Spin Driving by g-Matrix Modulation in Spin-Orbit Qubits, Phys. Rev. Lett. **120**, 137702 (2018).

[62] L. Bellentani, M. Bina, S. Bonen, A. Secchi, A. Bertoni, S. P. Voinigescu, A. Padovani, L. Larcher, and F. Troiani, Toward Hole-Spin Qubits in Si p-MOSFETs within a Planar CMOS Foundry Technology, Phys. Rev. Appl. **16**, 054034 (2021).

[63] B. Venitucci, L. Bourdet, D. Pouzada, and Y.-M. Niquet, Electrical manipulation of semiconductor spin qubits within the g-matrix formalism, Phys. Rev. B **98**, 155319 (2018).

[64] Y. Kato, R. C. Myers, D. C. Driscoll, A. C. Gossard, J. Levy, and D. D. Awschalom, Gigahertz electron spin manipulation using voltage-controlled g-tensor modulation, Science **299**, 1201 (2003).

[65] C. Adelsberger, S. Bosco, J. Klinovaja, and D. Loss, Enhanced orbital magnetic field effects in Ge hole nanowires, arXiv:2207.12050 (2022).

[66] J. Klinovaja and D. Loss, Composite Majorana fermion wave functions in nanowires, Phys. Rev. B **86**, 085408 (2012).

[67] The signs of the g-factors can be understood from Eq. (28) by considering a rotation of $\pi/2$ around y that transforms $\sigma_x \to \sigma_z$ and $\sigma_z \to -\sigma_x$. In addition, at large E_x, because of the SOI $\Delta\cos(\theta_z)\sigma_x p_\varphi$ in the effective Hamiltonian (25), the expectation value of mp_φ/m_φ in the harmonic oscillator ground state exactly cancels the SOI-induced Zeeman energy $\propto \tilde{\kappa}$ in the estimation of g_{zz}. One also finds that $\cos(\varphi)\sigma_{y,z} \to \pm e^{-\varphi_E^2(\varphi_S^{-2}+1/4)}\cosh(\varphi_E^2/\varphi_S)\sigma_{y,x}$ and $\sin(\varphi)\sigma_{y,z} \to e^{-\varphi_E^2(\varphi_S^{-2}+1/4)}\sinh(\varphi_E^2/\varphi_S)\sigma_{x,y}$.

[68] N. Ares, V. N. Golovach, G. Katsaros, M. Stoffel, F. Fournel, L. I. Glazman, O. G. Schmidt, and S. De Franceschi, Nature of Tunable Hole g Factors in Quantum Dots, Phys. Rev. Lett. **110**, 046602 (2013).

[69] C. Adelsberger, M. Benito, S. Bosco, J. Klinovaja, and D. Loss, Hole-spin qubits in Ge nanowire quantum dots: Interplay of orbital magnetic field, strain, and growth direction, Phys. Rev. B **105**, 075308 (2022).

[70] I. L. Drichko, A. A. Dmitriev, V. A. Malysh, I. Y. Smirnov, H. von Känel, M. Kummer, D. Chrastina, and G. Isella, Effective g factor of 2D holes in strained Ge quantum wells, J. Appl. Phys. **123**, 165703 (2018).

[71] J. H. Qvist and J. Danon, Anisotropic g-tensors in hole quantum dots: Role of transverse confinement direction, Phys. Rev. B **105**, 075303 (2022).

[72] F. Maier, C. Kloeffel, and D. Loss, Tunable g factor and phonon-mediated hole spin relaxation in Ge/Si nanowire quantum dots, Phys. Rev. B **87**, 161305 (2013).

[73] J. Li, B. Venitucci, and Y.-M. Niquet, Hole-phonon interactions in quantum dots: Effects of phonon confinement and encapsulation materials on spin-orbit qubits, Phys. Rev. B **102**, 075415 (2020).

[74] X. Hu and S. Das Sarma, Charge-Fluctuation-Induced Dephasing of Exchange-Coupled Spin Qubits, Phys. Rev. Lett. **96**, 100501 (2006).

[75] G. Burkard, T. D. Ladd, J. M. Nichol, A. Pan, and J. R. Petta, Semiconductor spin qubits, arXiv:2112.08863 (2021).

[76] Y. Makhlin, G. Schön, and A. Shnirman, Dissipative effects in Josephson qubits, Chem. Phys. **296**, 315 (2004).

[77] L. Cywiński, R. M. Lutchyn, C. P. Nave, and S. Das Sarma, How to enhance dephasing time in superconducting qubits, Phys. Rev. B **77**, 174509 (2008).

[78] If μ is the chemical potential of the dot, $\partial_V g_{ii} = \alpha\partial_\mu g_{ii} \approx \alpha\delta_{ii}^x g_{ii}/\hbar\omega_\varphi$. We use here the definition of the lever arm $\alpha = \partial\mu/\partial V$ [75], of $\delta g_{ii}^x = \hbar\omega_\varphi \partial_{E_x} g_{ii}/eR$, and we assume that the variation of the chemical potential μ are caused only by E_x, i.e., $\Delta\mu \approx eE_x R$.

[79] J. Yoneda, K. Takeda, T. Otsuka, T. Nakajima, M. R. Delbecq, G. Allison, T. Honda, T. Kodera, S. Oda, Y. Hoshi, N. Usami, K. M. Itoh, and S. Tarucha, A quantum-dot spin qubit with coherence limited by charge noise and fidelity higher than 99.9%, Nat. Nanotechnol. **13**, 102 (2018).

[80] F. H. L. Koppens, K. C. Nowack, and L. M. K. Vandersypen, Spin Echo of a Single Electron Spin in a Quantum Dot, Phys. Rev. Lett. **100**, 236802 (2008).

[81] H. Bluhm, S. Foletti, I. Neder, M. Rudner, D. Mahalu, V. Umansky, and A. Yacoby, Dephasing time of gaas electron-spin qubits coupled to a nuclear bath exceeding 200μs, Nat. Phys. **7**, 109 (2011).

[82] V. N. Golovach, M. Borhani, and D. Loss, Electric-dipole-induced spin resonance in quantum dots, Phys. Rev. B **74**, 165319 (2006).

[83] B. Voisin, V.-H. Nguyen, J. Renard, X. Jehl, S. Barraud, F. Triozon, M. Vinet, I. Duchemin, Y.-M. Niquet, S. de Franceschi, and M. Sanquer, Few-electron edge-state quantum dots in a silicon nanowire field-effect transistor, Nano Lett. **14**, 2094 (2014).

[84] A. C. Betz, M. L. V. Tagliaferri, M. Vinet, M. Broström, M. Sanquer, A. J. Ferguson, and M. F. Gonzalez-Zalba, Reconfigurable quadruple quantum dots in a silicon nanowire transistor, Appl. Phys. Lett. **108**, 203108 (2016).

[85] T. Lundberg, J. Li, L. Hutin, B. Bertrand, D. J. Ibberson, C.-M. Lee, D. J. Niegemann, M. Urdampilleta, N. Stelmashenko, T. Meunier, J. W. A. Robinson, L. Ibberson, M. Vinet, Y.-M. Niquet, and M. F. Gonzalez-Zalba, Spin quintet in a silicon double quantum dot: Spin blockade and relaxation, Phys. Rev. X **10**, 041010 (2020).

[86] O. Dmytruk, D. Chevallier, D. Loss, and J. Klinovaja, Renormalization of the quantum dot g-factor in superconducting Rashba nanowires, Phys. Rev. B **98**, 165403 (2018).

[87] P. M. Mutter and G. Burkard, Natural heavy-hole flopping mode qubit in germanium, Phys. Rev. Res. **3**, 013194 (2021).

[88] S. M. Girvin, Circuit QED: Superconducting qubits coupled to microwave photons, Quantum machines: measurement and control of engineered quantum systems, 113 (2014).

[89] A. Blais, A. L. Grimsmo, S. M. Girvin, and A. Wallraff, Circuit quantum electrodynamics, Rev. Mod. Phys. **93**, 025005 (2021).

[90] A. R. Mills, C. R. Guinn, M. J. Gullans, A. J. Sigillito, M. M. Feldman, E. Nielsen, and J. R. Petta, Two-qubit silicon quantum processor with operation fidelity exceeding 99%, Sci. Adv. **8**, eabn5130 (2022).

[91] A. M. J. Zwerver *et al.*, Qubits made by advanced semiconductor manufacturing, Nat. Electron. **5**, 184 (2022).

[92] J. J. Viennot, J. Palomo, and T. Kontos, Stamping single wall nanotubes for circuit quantum electrodynamics, Appl. Phys. Lett. **104**, 113108 (2014).

[93] M. Hagmann, Isolated carbon nanotubes as high-impedance transmission lines for microwave through terahertz frequencies, IEEE Trans. Nanotechnol. **4**, 289 (2005).

[94] J. D. Chudow, D. F. Santavicca, and D. E. Prober, Terahertz spectroscopy of individual single-walled carbon nanotubes as a probe of luttinger liquid physics, Nano Lett. **16**, 4909 (2016).

[95] S. Bosco and D. P. DiVincenzo, Transmission lines and resonators based on quantum Hall plasmonics: Electromagnetic field, attenuation, and coupling to qubits, Phys. Rev. B **100**, 035416 (2019).

[96] S. Bosco, D. DiVincenzo, and D. Reilly, Transmission Lines and Metamaterials Based on Quantum Hall Plasmonics, Phys. Rev. Appl. **12**, 014030 (2019).

[97] S. J. Elman, S. D. Bartlett, and A. C. Doherty, Long-range entanglement for spin qubits via quantum Hall edge modes, Phys. Rev. B **96**, 115407 (2017).

[98] A. Gourmelon, H. Kamata, J.-M. Berroir, G. Fève, B. Plaçais, and E. Bocquillon, Characterization of helical luttinger liquids in microwave stepped-impedance edge resonators, Phys. Rev. Res. **2**, 043383 (2020).

[99] M. Lodari, O. Kong, M. Rendell, A. Tosato, A. Sammak, M. Veldhorst, A. R. Hamilton, and G. Scappucci, Lightly strained germanium quantum wells with hole mobility exceeding one million, Appl. Phys. Lett. **120**, 122104 (2022).

[100] G. L. Bir and G. E. Pikus, *Symmetry and Strain-Induced Effects in Semiconductors* (Wiley, New York, 1974), Vol. 484.

[101] L. D. Landau and E. M. Lifshitz, *Course of Theoretical Physics: Theory of Elasticity* (Pergamon, New York, 1970), Vol. 7.

[102] J. Grönqvist, N. Søndergaard, F. Boxberg, T. Guhr, S. Åberg, and H. Q. Xu, Strain in semiconductor core-shell nanowires, J. Appl. Phys. **106**, 053508 (2009).

[103] N. Nishiguchi, Confined and interface acoustic phonons in a quantum wire, Phys. Rev. B **50**, 10970 (1994).

[104] M. Povolotskyi and A. Di Carlo, Elasticity theory of pseudomorphic heterostructures grown on substrates of arbitrary thickness, J. Appl. Phys. **100**, 063514 (2006).